Seismic evidence for fluids in fault zones on top of the subducting Cocos Plate beneath Costa Rica

Harm J. A. Van Avendonk,[1] W. Steven Holbrook,[2] Daniel Lizarralde,[3] Mauricio M. Mora,[4] Steven Harder,[5] Andrew D. Bullock,[2] Guillermo E. Alvarado[4,6] and Carlos J. Ramírez[4]

[1]*University of Texas Institute for Geophysics, Austin,* TX 78758, *USA. E-mail: harm@ig.utexas.edu*
[2]*Department of Geology and Geophysics, University of Wyoming, Laramie,* WY 82071, *USA*
[3]*Woods Hole Oceanographic Institution, Department of Geology and Geophysics, Woods Hole,* MA 02543, *USA*
[4]*Escuela Centroamericana de Geología, University of Costa Rica, San Pedro* 214-2060, *Costa Rica*
[5]*University of Texas at El Paso, Department of Geological Sciences, El Paso,* TX 79968, *USA*
[6]*Instituto Costarricense de Electricidad, San José* 10032-1000, *Costa Rica*

SUMMARY
In the 2005 TICOCAVA explosion seismology study in Costa Rica, we observed crustal turning waves with a dominant frequency of $\sim$10 Hz on a linear array of short-period seismometers from the Pacific Ocean to the Caribbean Sea. On one of the shot records, from Shot 21 in the backarc of the Cordillera Central, we also observed two seismic phases with an unusually high dominant frequency ($\sim$20 Hz). These two phases were recorded in the forearc region of central Costa Rica and arrived $\sim$7 s apart and 30–40 s after the detonation of Shot 21. We considered the possibility that these secondary arrivals were produced by a local earthquake that may have happened during the active-source seismic experiment. Such high-frequency phases following Shot 21 were not recorded after Shots 22, 23 and 24, all in the backarc of Costa Rica, which might suggest that they were produced by some other source. However, earthquake dislocation models cannot produce seismic waves of such high frequency with significant amplitude. In addition, we would have expected to see more arrivals from such an earthquake on other seismic stations in central Costa Rica. We therefore investigate whether the high-frequency arrivals may be the result of a deep seismic reflection from the subducting Cocos Plate. The timing of these phases is consistent with a shear wave from Shot 21 that was reflected as a compressional ($S{\times}P$) and a shear ($S{\times}S$) wave at the top of the subducting Cocos slab between 35 and 55 km depth. The shift in dominant frequency from $\sim$10 Hz in the downgoing seismic wave to $\sim$20 Hz in the reflected waves requires a particular seismic structure at the interface between the subducting slab and the forearc mantle to produce a substantial increase in reflection coefficients with frequency. The spectral amplitude characteristics of the $S{\times}P$ and $S{\times}S$ phases from Shot 21 are consistent with a very high V_p/V_s ratio of 6 in $\sim$5 m thick, slab-parallel layers. This result suggests that a system of thin shear zones near the plate interface beneath the forearc is occupied by hydrous fluids under near-lithostatic conditions. The overpressured shear zone probably takes up fluids from the downgoing slab, and it may control the lower limit of the seismogenic zone.

Key words: Controlled source seismology; Body waves; Wave propagation; Subduction zone processes; Continental margins: convergent.

GJI Seismology

1 INTRODUCTION

Some of the largest earthquakes occur at subduction zones, where strain is accumulated and released at the contact between the two converging tectonic plates. Seismic studies have shown that these seismogenic zones often do not extend deeper than the base of the forearc crust (DeShon *et al.* 2003; DeShon & Schwartz 2004). Beneath this depth, it has been speculated that hydrous minerals, such as serpentine and talc, enable steady or transient creep at the plate interface between oceanic lithosphere and the mantle wedge (Hyndman & Peacock 2003; Hilairet *et al.* 2007). Alternatively, high fluid pressures due to dehydration of these minerals may reduce the friction across this interface (Kodaira *et al.* 2004; Moore & Lockner 2007). Improving our understanding of the rheology and intermediate-depth seismogenic processes at convergent plate boundaries primarily requires direct

997

observations of the release and transport of fluids within the subduction system.

Prograde metamorphic reactions cause the release of volatiles from the oceanic crust and upper mantle as they are subducted and subjected to increasing pressure and temperature (Bebout 2007). The transformation from blueschist to eclogite facies in the oceanic crust and the breakdown of serpentinite in the upper mantle of the downgoing plate may be the most important sources of water deep in the subduction zone (Rüpke *et al.* 2004; Peacock *et al.* 2005). Fluids released from downgoing slabs into the mantle wedge affect subduction zone processes at a variety of scales. Fluids that are absorbed by the overlying mantle wedge will alter its viscosity, thereby exerting a control on mantle flow and temperature structure (Manea & Gurnis 2007). Water that is subducted to depths of ∼100 km can lead to mantle melting beneath volcanic arcs (Schmidt & Poli 1998). If the permeability of the mantle wedge corner is low (Mibe *et al.* 1999), or if the plate interface itself forms an impermeable seal (Audet *et al.* 2009), water expelled from the downgoing plate may become trapped at the slab interface. The possible presence of free water here has great implications for the rheology of the megathrust and the conditions that may result in slow-slip events (Shelly *et al.* 2006; Moore & Lockner 2007; Liu & Rice 2007).

The structure of the shear zone between the two plates has been investigated extensively in exhumed, ancient high-pressure and ultrahigh-pressure terranes (Bebout 2007). These studies show that water released during prograde metamorphism chemically altered fault zones, but not much of the surrounding rock of the downgoing oceanic lithosphere (Barnicoat & Cartwright 1995; Spandler *et al.* 2003). This observation suggests a strong relationship between fluid flow and fault slip near the plate interface. Unfortunately, some of the context of ancient subduction zones is unknown, such as the age and speed of descending lithosphere. Seismic imaging of high V_p/V_s in modern subduction zones provides evidence of elevated fluid pressures in the slab beneath the forearc of Nicaragua, Mexico, Japan, and British Columbia (Abers *et al.* 2003; Kodaira *et al.* 2004; Audet *et al.* 2009; Song *et al.* 2009) that likely originate from dehydration reactions in the downgoing plate. The long seismic wavelengths used in most of these studies make it difficult to distinguish hydrous fluids in discrete fault zones from fluids distributed throughout the subducting crust.

In this study we show deep seismic phases from a seismic refraction study in central Costa Rica that have distinct frequency and amplitude characteristics, which may enable us to infer physical properties of the slab–mantle interface beneath the forearc. Such *in situ* seismic constraints can fill an important gap in our understanding of geological processes at the plate boundary at these intermediate depths.

2 TECTONIC SETTING

The arc and forearc of central Costa Rica form the western margin of the Caribbean Plate (Alvarado *et al.* 1997), which is a large igneous plateau that originated in the eastern Pacific (Hauff *et al.* 1997). Miocene (22 Ma) to present subduction of the Farallon Plate and Cocos Plate (Vogel *et al.* 2004; Mann *et al.* 2007) resulted in the construction of a volcanic arc with a thickness of 27–40 km (Sallarès *et al.* 2001; MacKenzie *et al.* 2008). The deep crustal structure of the arc, with compressional seismic velocities (V_p) varying from ∼6.0 km s^{-1} in the upper crust to ∼7.2 km s^{-1} in the lower crust (Sallarès *et al.* 2001; Husen *et al.* 2003), is indicative of a mafic composition. The partially serpentinized mantle wedge corner at depths to ∼50 km has seismic velocities that are not substantially higher than that of the lower arc crust (DeShon & Schwartz 2004; Syracuse *et al.* 2008). The subducted and metamorphosed oceanic crust of the Cocos Plate has a V_p of 7.0–7.5 km s^{-1} at depths of ∼50 km (Husen *et al.* 2003), which is also similar to that of the overriding lower arc crust and the mantle wedge corner. Tomographic images of the subduction zone are therefore not very helpful in distinguishing the deep structure of the forearc, but the depth of the interface between the top of the Cocos slab and the forearc mantle is fairly well illuminated by its seismicity (Syracuse & Abers 2006).

The oceanic lithosphere of the Cocos Plate that subducted beneath central Costa Rica formed at the Cocos-Nazca spreading centre. The Galapagos hotspot, which was located in the vicinity of this spreading centre since at least 20 Ma (Sallarès & Charvis 2003), produced the Cocos Ridge, which has been estimated to be 21 km (Walther 2003) and 18–19 km (Sallarès *et al.* 2003) thick. In addition, several large seamounts and plateaus formed outboard the Middle American Trench (von Huene *et al.* 2000; Fig. 1). Collision
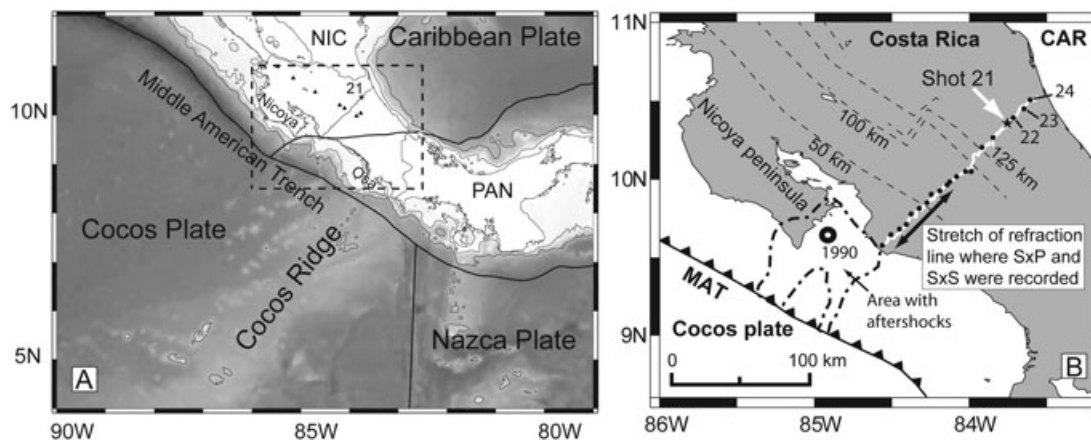

Figure 1. (a) Tectonic map of southern Central America. NIC, Nicaragua; PAN, Panama; 21, Shot 21. Volcanoes in Costa Rica are marked as black triangles. (b) Location map of the 2005 TICOCAVA experiment in Costa Rica. MAT, Middle American Trench; CAR, Caribbean Plate. Dashed lines are depth contours of the Cocos Plate beneath Costa Rica (Syracuse & Abers 2006). Black circles indicate explosions from the seismic study. Shot 21 is marked with a star. Shots 22, 23 and 24 are marked with annotated black circles. White line marks the array of vertical-component seismometers. Open circle offshore marks the location of the 1990 March 25, earthquake and its aftershock area (dash-dotted outline) (Protti *et al.* 1995).

of this thickened oceanic crust with the overriding plate caused uplift and tectonic erosion of the Costa Rica margin (Vannucchi *et al.* 2006; LaFemina *et al.* 2009; Sak *et al.* 2009) since the last 2–3 Ma (MacMillan *et al.* 2004). The seafloor that currently lies outboard of the trench offshore central Costa Rica is approximately 18–22 Ma old (Barckhausen *et al.* 2001), and it is converging with the stable interior of the Caribbean plate at 8.5 mm yr^{-1} at a 20° angle from the orthogonal direction (DeMets 2001).

The seamounts on the subducting seafloor offshore central Costa Rica appear to moderate the magnitude of thrust earthquakes (Bilek *et al.* 2003), because these asperities form rupture surfaces of limited size. Some of the largest earthquakes reported in the region are the 1983 Osa ($M_w = 7.3$) earthquake (Adamek *et al.* 1987), the 1990 Gulf of Nicoya ($M_w = 7.0$) earthquake (Protti *et al.* 1995) and the 1999 ($M_w = 6.9$) Quepos earthquake (Bilek & Lithgow-Bertelloni 2005). Husen *et al.* (2002) show a seismic velocity image of an asperity in the opening of the Gulf of Nicoya that may have slipped during the 1990 earthquake. Each of these historic earthquakes offshore central Costa Rica is smaller than the 1950 ($M_w = 7.7$) Nicoya Peninsula earthquake (DeShon *et al.* 2006). The smoother seafloor offshore northern Nicoya Peninsula and farther northwest toward Nicaragua is believed to provide stronger coupling between the two plates in the seismogenic zone (Bilek *et al.* 2003; DeShon *et al.* 2006).

Microseismicity in central Costa Rica is mostly located in the vicinity of the subducting Cocos Plate and in the upper crust of the volcanic front (Protti *et al.* 1994; Husen *et al.* 2003; DeShon *et al.* 2006). The upper crust near the Pacific coast of central Costa Rica shows less seismic activity (Protti *et al.* 1995; Quintero & Güendel 2000). Recent seismicity and geodetic studies have found areas of the slab interface with increased seismicity (DeShon *et al.* 2003, 2006) and locked patches (Norabuena *et al.* 2004; Ghosh *et al.* 2008) that could rupture as a large earthquake. The deeper limit of this complex seismogenic zone is estimated to range from ∼26 km in the southern Nicoya peninsula to ∼35 km near the Osa peninsula (DeShon *et al.* 2003, 2006), which is not much different from the depth of the Moho beneath the forearc (MacKenzie *et al.* 2008). This coincidence suggests that the juxtaposition of serpentinites from the outer corner of the mantle wedge and downgoing oceanic lithosphere creates a stable sliding regime at the slab interface (DeShon *et al.* 2006).

3 DATA

3.1 Deep seismic phases

During the 2005 Transects to Investigate the Crustal Origin of the Central American Volcanic Arc (TICOCAVA) experiment, we recorded a total of 37 explosions on an array of 748 vertical-component seismometers from the U.S. national seismic instrumentation facility IRIS/PASSCAL. The seismic array was first deployed along a line from the Pacific across the volcanic arc near Barva volcano to the Caribbean coast, and it was subsequently moved to a transect along the volcanic front from the Nicaraguan border to Irazú volcano. The 154-km-long refraction line across the volcanic arc had an average instrument spacing of 200 m (Fig. 1). Most of the observed seismic arrivals were compressional waves, but we also recorded some excellent shear wave arrivals in this experiment.

Shot 21, which was located 45 km northeast of the volcanic arc on the first transect, appears to have generated two strong, deep seismic phases with a dominant frequency of approximately 20 Hz.

The frequency content is much higher than the ∼10 Hz average frequency of the turning waves from Shot 21 and other explosions (Fig. 2a). The two phases were recorded on approximately 300 instruments in the forearc of central Costa Rica at source–receiver offsets between 70 and 125 km. No such deep phases were recorded in the northeastern arc and backarc portion of this shot gather. A clear compressional turning wave (P_g) and a faint shear turning wave (S_g) from Shot 21 appear at offsets that are consistent with an existing regional seismic velocity model (Husen *et al.* 2003).

The arrival times of the deep seismic phases of Shot 21 are consistent with that of a shear wave converted to a compressional wave ($S{\times}P$) and a shear-to-shear converted wave ($S{\times}S$) from the subducting Cocos slab. If the corner of the mantle wedge in central Costa Rica is serpentinized by ∼15% (DeShon *et al.* 2003), which corresponds to a compressional velocity (V_p) of ∼7.2 km s^{-1} and a shear velocity (V_s) of 4.0 km s^{-1} (Hacker *et al.* 2003; Christensen 2004), we can fit the arrival times of the $S{\times}P$ and $S{\times}S$ phases mostly within 1 s (Fig. 3). This traveltime fit is an indication that the $S{\times}P$ and $S{\times}S$ phases bounced off an interface that lies within no more than a few km of the top of the Wadati-Benioff zone at depths between 35 and 55 km (Syracuse & Abers 2006). Arroyo *et al.* (2009) recently interpreted the top of low seismic velocity anomaly in their tomographic image as the slab interface beneath the Pacific coast of Costa Rica. However, at depths greater than 40 km, the slab seismicity, which extends to 200 km (Protti *et al.* 1994; Syracuse & Abers 2006) outlines a boundary that lies approximately 10 km deeper. In our study we use the slab interface parameterization of Syracuse & Abers (2006), which shows a smoother bend in the downgoing Cocos Plate beneath the forearc mantle. At depths shallower than 40 km there is less ambiguity in the depth of the slab interface (Fig. 3). Given that the forearc crust here is roughly 30 km thick (DeShon *et al.* 2003; DeShon & Schwartz 2004; MacKenzie *et al.* 2008), the wave paths of the reflections must traverse the upper 5–25 km of the outer corner of the mantle wedge.

Unfortunately, the $S{\times}P$ and $S{\times}S$ phases were not observed in other shot records of the TICOCAVA study. Shots 22, 23 and 24 (Figs 2b–d), located farther northeast in the backarc of the Cordillera Central (Fig. 1b), recorded P_g and S_g, but not the $S{\times}P$ and $S{\times}S$ phases. Interpreting the $S{\times}P$ and $S{\times}S$ phases of Shot 21 as slab reflections therefore implies that the explosions do not consistently produce detectable shear-wave reflections from the subducting slab. Shot 24 recorded a weak compressional wave reflecting off the subducting slab ($P{\times}P$), which does not have the high-frequency character of $S{\times}P$ and $S{\times}S$ in the record of Shot 21.

3.2 Seismicity

The traveltimes of the $S{\times}P$ and $S{\times}S$ phases of Shot 21 are consistent with the best existing estimates for the position of the slab (Syracuse & Abers 2006) and for mantle-wedge seismic velocities (Husen *et al.* 2003), so our explanation of these phases as slab reflections is in some sense the simplest interpretation. The $S{\times}P$ and $S{\times}S$ phases are very clear seismic arrivals, but the absence of such phases in other TICOCAVA shot records requires inspection of time-series from other seismic stations that were operating during the detonation of Shot 21.

An alternative explanation for the deep seismic phases is that a small earthquake might have occurred right after the detonation of Shot 21. Given the high seismicity at the Wadati-Benioff zone of the subducting Cocos Plate, the most likely place for such an event would be beneath the forearc at depths between 15 and 40 km.
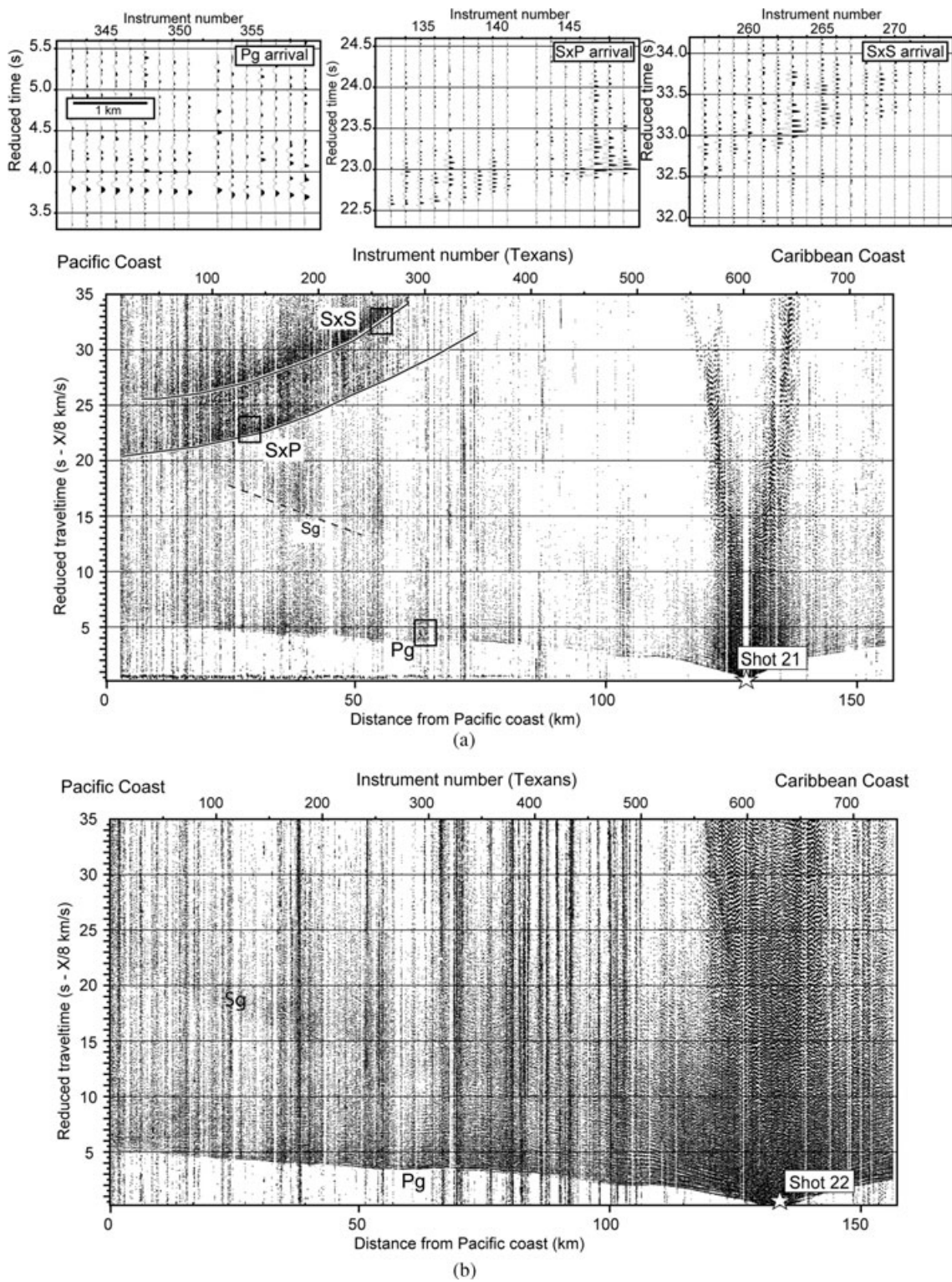
Figure 2. (a) Shot 21 gather of seismic refractions. The main diagram shows all seismic phases (P_g, S_g, $S{\times}P$ and $S{\times}S$) with a reduction velocity of 8 km s^{-1}. The three black squares mark the location of the enlargements (P_g, $S{\times}P$ and $S{\times}S$) of three panels above; X is the source–receiver distance. (b) Vertical-component receiver gather of Shot 22. The locations of all shots are marked in Fig. 1(b). The horizontal and vertical axes are as in (a). (c) Shot 23 lies northeast of both Shots 21 and 22. Besides the turning waves P_g and S_g, we interpret a reflection from the arc Moho (PmP). (d) Shot 24 was located near the Caribbean coast, at the largest distance from the subducting Cocos slab. The inset shows an enlargement of the box inside the receiver gather, with a phase that we interpret as $P{\times}P$.
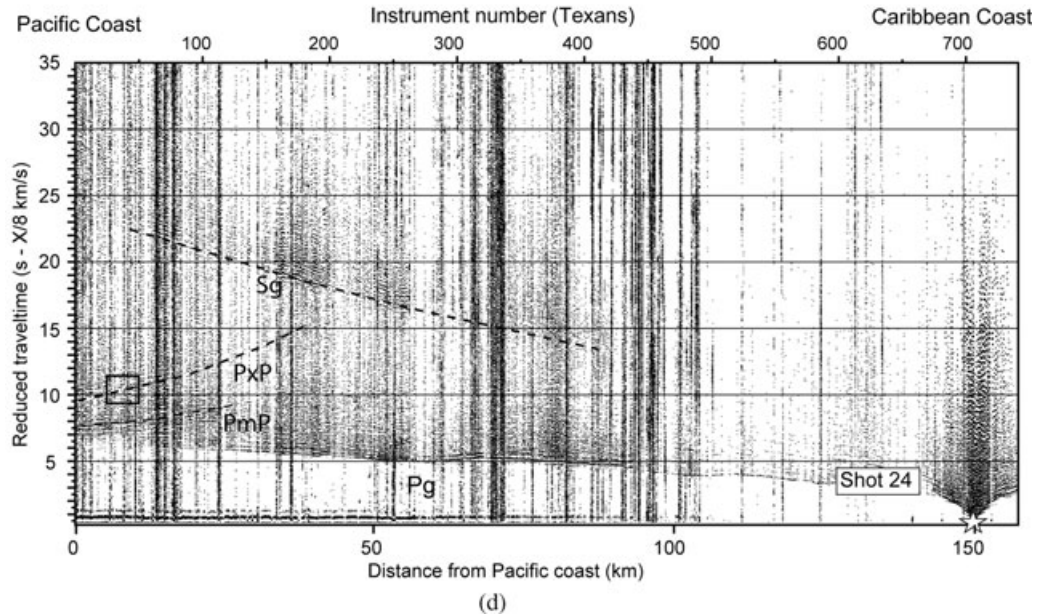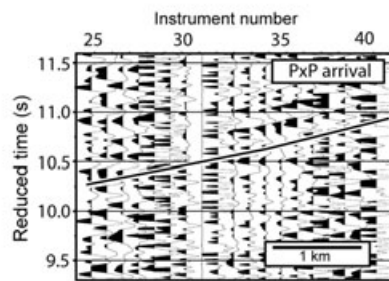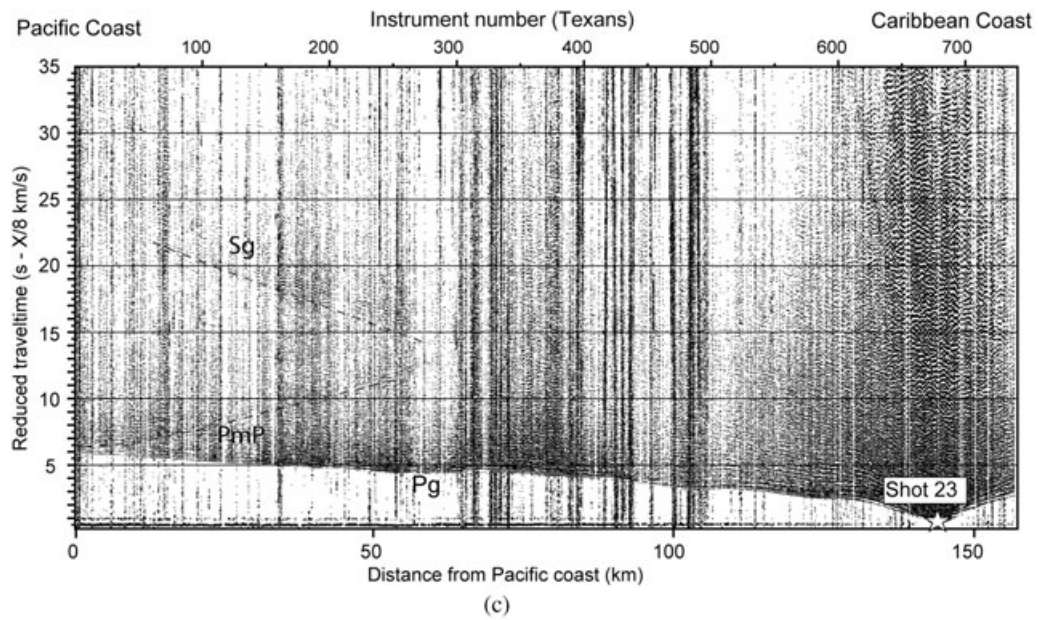
Figure 2. (*Continued.*)

However, ray tracing shows that if an event occurred in the seismogenic zone near the Pacific coast of Costa Rica, the traveltime branches of P_g and S_g would have a steeper slope than the $S \times P$ and $S \times S$ observed in our data (Fig. 4a). On the other hand, an earthquake could produce P_g and S_g waves that are consistent with $S \times P$ and $S \times S$ in the TICOCAVA data if this secondary event occurred

near the slab interface beneath the forearc mantle at a distance of ~40 km from the Pacific coast and at a depth of ~52 km (location Q in Fig. 4b and in Fig. 5), roughly 25 s after Shot 21 was fired. This scenario fits both the $S \times P$ (P_g) and $S \times S$ (S_g) phases fairly well. The alternative source may also lie outside the plane of our refraction profile in the forearc. In that case the earthquake would
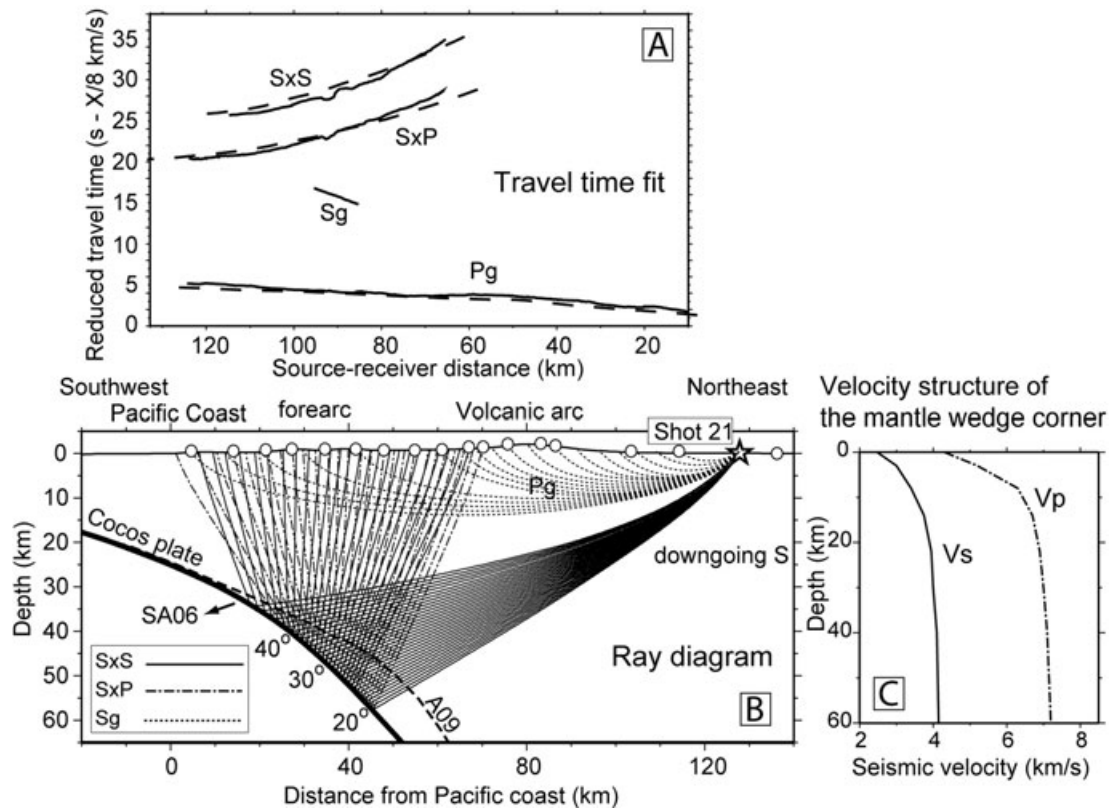
Figure 3. (a) Traveltime fit of the $S \times P$ and $S \times S$ phases of Shot 21. (b) Ray diagram along the seismometer array with Cocos slab surface SA06 (Syracuse & Abers 2006), which we use in this paper. The slab interface inferred by Arroyo *et al.* (2009) from their tomographic seismic velocity model is indicated by a dashed line. Shot 21 is marked with a star. Other shots are marked with a circle. The angle of incidence of shear waves at the slab–mantle interface is indicated in 10° increments. (c) The ray paths were traced in an existing seismic velocity model (Husen *et al.* 2003).
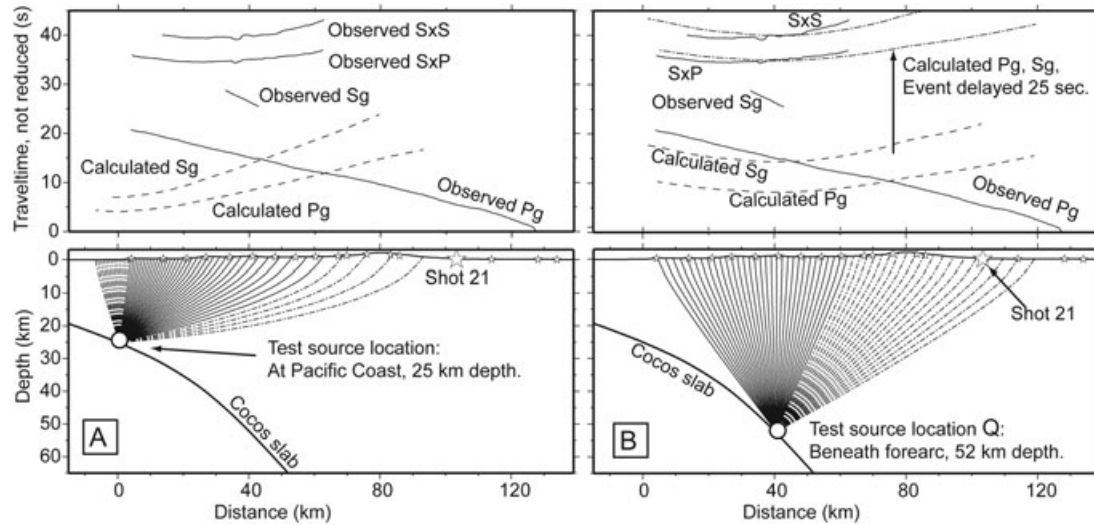

Figure 4. Ray tracing tests for two scenarios with a secondary source during Shot 21. (a) If a secondary source is placed at the plate boundary near the Pacific coast (bottom), we calculate traveltime curves (dashed lines, above) that have a steeper slope than the observed $S \times S$ and $S \times P$ arrivals. (b) Diagram with traveltimes of phases observed after Shot 21 (solid lines). If the secondary source is placed at the plate interface at 52 km depth, calculated traveltime slopes are flatter (dashed lines). If this secondary event, which we label Q, was ~25 s after Shot 21 (dash-dotted curves), its P and S waves would match $S \times P$ and $S \times S$ quite well. In both (a) and (b), we have dash-dotted ray paths where we did not observe $S \times S$ and $S \times P$.

have to be shallower, because the total length of the path between the source and receivers is constrained by the ~7 s time gap between the incoming $S \times P$ (P_g) and $S \times S$ (S_g) phases. Microseismicity beneath the forearc of central Costa Rica is mostly confined to the subducting oceanic crust and the upper 20 km of the forearc crust

(Husen *et al.* 2003). Besides location Q at 52 km depth on our refraction line, a small earthquake in the upper crust of the forearc to the northwest (Q_{NW}) or southeast (Q_{SE}) could perhaps also have produced $S \times P$ and $S \times S$ (Fig. 5). Regardless of the location of their source, there is no ambiguity between the timing of the event and
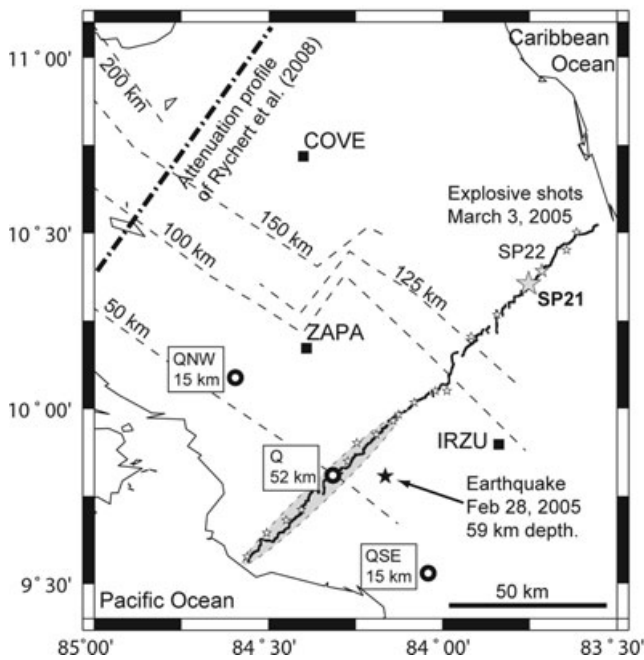
Figure 5. Map of our study in central Costa Rica. Black solid line shows TICOCAVA array of seismometers, with the area where $S{\times}P$ and $S{\times}S$ were observed shaded in grey. Explosive shots are marked by light grey stars. The black star indicates a local earthquake. The open circles mark the locations of a hypothesized earthquake at Q_{NW}, Q (also shown in Fig. 4b) and Q_{SE}. TUCAN instruments are indicated by solid black squares. The attenuation profile (Rychert *et al.* 2008) used in our study is indicated with a dash-dotted line. Cocos slab contours (Syracuse & Abers 2006) are drawn as thin dashed lines.

the distance that the $S{\times}P$ and $S{\times}S$ phases travelled to our instruments. If these phases were not converted reflections from the slab, they must come from a separate event that occurred approximately 25 s after Shot 21.

A small earthquake with an origin time 25 s after Shot 21 on 2005 March 3 in central Costa Rica might be registered by permanent and temporary seismic arrays. However, the earthquake catalogue derived from the Costa Rican monitoring network does not identify such an event following shortly after Shot 21. If the TICOCAVA short-period instrument array recorded a small earthquake in this location Q (Fig. 5), we would expect to see this event on stations in the northeastern half of this array (Fig. 2a). The ray diagram of Fig. 4(b) shows that direct waves from a source beneath the forearc mantle can easily reach the arc and backarc region of our refraction profile, however we did not observe the high-frequency phases here (Fig. 4b). We also inspected data from the TUCAN broadband seismic array (G.A. Abers, personal communication, 2008), which was also operating in 2005, for possible arrivals from a microearthquake during Shot 21. A few of the TUCAN stations were placed relatively close to Shot 21 and the TICOCAVA array (Fig. 5). Time-series and spectra from the vertical component of Shot 21 from TUCAN broadband stations ZAPA, IRZU and COVE, all recording at 50 samples s^{-1}, are shown in Fig. 6. The TUCAN data confirm that the S_g arrival of Shot 21 was weak compared to P_g, because S_g is only visible on one of these instruments. A low-amplitude arrival '*a*' followed 38 s after P_g on ZAPA, and two small arrivals '*b*' and '*c*' came in on COVE, 28 and 39 s after P_g, respectively. These arrivals do not appear as prominent as the $S{\times}P$ and $S{\times}S$ phases in the TICOCAVA data, but we nevertheless test whether they may be direct arrivals from one of the alternative

source locations Q, Q_{NW} and Q_{SE} (Fig. 5). The '*a*' arrival on ZAPA is later than any P or S traveltime from Q, Q_{NW} or Q_{SE}. Station IRZU does not show any events after the P_g from Shot 21. Event '*b*' on station COVE coincides nicely with the expected P arrival time from Q, but a second event '*c*' recorded by COVE is too early to represent the S arrival from Q. The other locations Q_{NW} and Q_{SE} do not predict the arrival of '*b*' or '*c*'. We conclude that $S{\times}P$ and $S{\times}S$ were only observable in the forearc, where the southwestern portion of the TICOCAVA array registered these arrivals. If there had been a small earthquake $\sim$25 s after Shot 21, we would expect the TUCAN instruments to show prominent P and S arrival at various different azimuths in central Costa Rica from that event, in a similar fashion as the event of 2005 February 28 (Fig. 7). This small ($M_w \sim 2$) earthquake occurred at 59 km depth near the slab interface, just 10 km from the TICOCAVA array (Fig. 5). The event of February 28 shows that small earthquakes from this approximate location can produce a P and S wave that arrive within 12–20 s on stations ZAPA, IRZU and COVE.

A comparison between the spectra of $S{\times}P$ and $S{\times}S$ phases (Fig. 8) and the spectrum of the small earthquake of 2005 February 28 shows that the latter contains much lower frequencies. The steady decrease in spectral amplitude of the earthquake with frequency between 5 and 10 Hz (Fig. 7) may be consistent with an upper corner frequency at 5 Hz or less, which would correspond to an event with a magnitude M_w of at least 2 (Aki 1967). An event of this size may just be large enough to be recorded across the TUCAN network (G.A. Abers, personal communication, 2009), as was the case for this small earthquake. According to a circular dislocation model (Sato & Hirasawa 1973), a corner frequency of 5 Hz corresponds to a fault rupture with a diameter smaller than 1 km. For higher corner frequencies, the requisite fault sizes and earthquake magnitudes are even smaller (Aki 1967; Sato & Hirasawa 1973). The spectra of the $S{\times}P$ and $S{\times}S$ phases of Shot 21 are much more sharply peaked than those of a normal earthquake (Aki 1967), so we cannot distinguish a lower and upper corner frequency for this event. If we nevertheless interpret the peak frequency at 20 Hz (Fig. 8) as the upper corner frequency of a seismic dislocation, its magnitude would probably have to be smaller than 0. In that case the event would not be recorded over $\sim$100 km, as we did in the TICOCAVA study, so the earthquake dislocation model does not apply well to the $S{\times}P$ and $S{\times}S$ phases. This strengthens our interpretation that these phases did not result from an earthquake but rather are reflection phases originating from Shot 21.

Based on our ray tracing and inspection of the TUCAN data, we assume that the $S{\times}P$ and $S{\times}S$ seismic phases in the TICOCAVA data originated from Shot 21 and not from a separate source, such as an earthquake. Presumably, the particular combination of shallow geology, site location, shot-hole geometry and explosive disposition within the shot hole were conducive to generating strong S-wave energy from Shot 21 with a directivity favourable for recording reflections from the slab on our seismometer array.

4 METHOD

4.1 Data analysis

We here investigate if the anomalously high frequencies of $S{\times}P$ and $S{\times}S$ phases of Shot 21 can be a response characteristic of the seismic velocity structure within a $\sim$1-km-thick zone at the boundary between the Cocos and Caribbean plates. To explain the observed discrepancy between dominant frequency of these deep phases ($\sim$20 Hz) and the crustal turning waves ($\sim$10 Hz), the
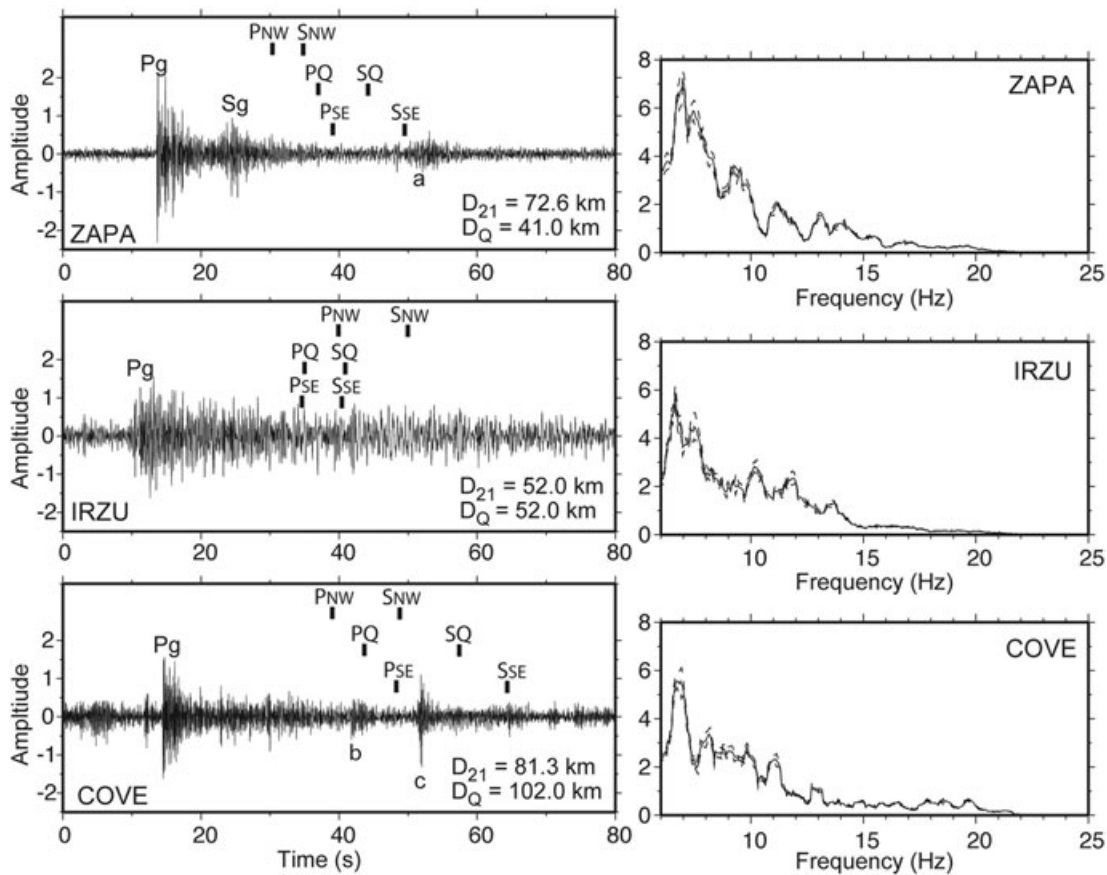
Figure 6. Vertical-component recording of three TUCAN stations of Shot 21. We identify the compressional and shear waves of this explosion with the labels P and S. The labels PQ and SQ and small black bars mark the predicted P and S arrival times for the hypothetical earthquake Q (for location, see Fig. 5) with an origin time 25 s after Shot 21. Similarly, we predict the P- and S-wave arrival for the source locations Q_{NW} and Q_{SE}. D_{21} and D_Q are epicentral distances to Shot 21 and Q. Events labelled a, b and c are discussed in the text. The spectra of these arrivals are shown on the right (solid curve) with 67% confidence levels indicated by dashed lines.

reflection coefficients of the plate interface must increase strongly with frequency. The ray diagram of Shot 21 (Fig. 3) shows that our data would constrain the S–P and S–S reflection coefficients over a range of incidence angles between 14° and 38°.

We may obtain the frequency-dependent reflection coefficients at the slab–mantle interface by comparing the spectra of the seismic wave that impinges on this boundary with the spectrum of the observed $S{\times}P$ and $S{\times}S$ reflections. We have no exact record of the wave from Shot 21 that reached the plate boundary, but we will assume that crustal refractions P_g and S_g have the same frequency content. We construct the spectra of wide-angle seismic refractions and reflections with a multitaper spectral analysis (Park *et al.* 1987; Percival & Walden 1998). The analysis confirms that the large difference in frequency content between the deeper phases $S{\times}P$ and $S{\times}S$ and crustal turning waves P_g and S_g is statistically significant (Fig. 8). Ideally, we would approximate the reflection coefficients by dividing the spectra of $S{\times}P$ and $S{\times}S$ by the spectrum of S_g. However, the signal-to-noise ratio of the S_g arrival of Shot 21 is much poorer than that of the other phases, as can be seen in the time-series of Fig. 8. It is therefore likely that the S_g spectrum that we measure at the surface is biased toward the background noise. To avoid this bias in our analysis, we assume that the compressional (P_g) and shear (S_g) waves from Shot 21 have very similar frequency content (Fig. 8), and estimate reflection coefficients by dividing the spectra of $S{\times}P$ and $S{\times}S$ by the spectrum of P_g.

Before we compare the observed reflection amplitudes with reflection coefficients calculated for seismic velocity models of the slab–mantle interface, we project our data from the Earth's surface onto the shear zone. The $S{\times}P$ and $S{\times}S$ arrivals span a distance of approximately 55 km along our refraction profile, from the Pacific coast to the volcanic arc, with the strongest of the $S{\times}P$ phase arriving near the coast, and most of the $S{\times}S$ phase arriving farther inland (Fig. 9a). Using the ray paths of the $S{\times}P$ and $S{\times}S$ phases in the seismic velocity model (Fig. 9b), we map these reflection amplitudes onto reflection points at the slab–mantle interface between depths of 35 and 55 km (Fig. 9c). The projection shows that the $S{\times}P$ and $S{\times}S$ reflection points cover a horizontal distance of just 25 km along the slab interface. Moreover, it appears that the spatial correlation of $S{\times}P$ and $S{\times}S$ amplitudes between 15 and 20 Hz is much better on top of the slab than at the Earth's surface (Fig. 9).

To interpret the variation in amplitude of the $S{\times}P$ and $S{\times}S$ phases along the array of vertical-component geophones, we must consider the polarization of particle motion for these two arrivals. The $S{\times}P$ particle motion is oriented in the direction of wave propagation as it approaches the instrument array, whereas $S{\times}S$ is polarized perpendicular to its wave path. Consequently, if $S{\times}P$ and $S{\times}S$ were direct P and S generated by a separate source beneath Costa Rica (location Q in Fig. 4b), we would expect to record highest $S{\times}P$ amplitudes inland, and we would see amplitudes decrease toward the Pacific coast where the incidence angle of ray
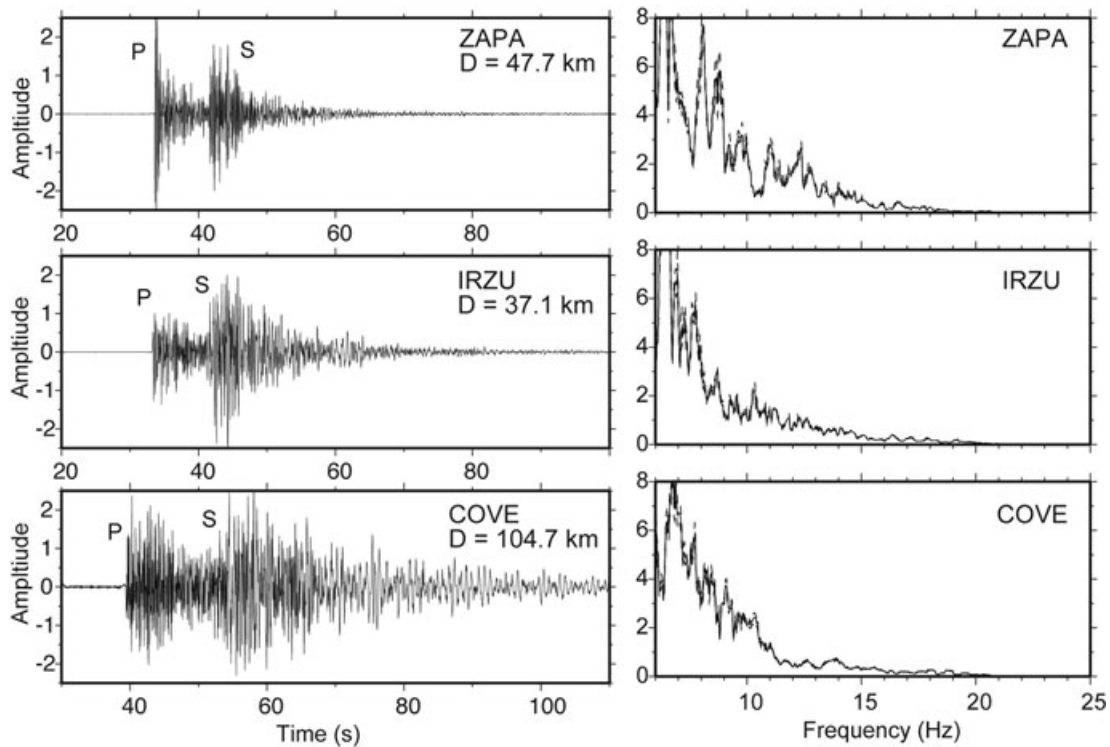
Figure 7. Vertical-component recording of three TUCAN stations of an earthquake on 2005 February 28. *D* is epicentral distance.

paths are larger. Conversely, the amplitude of a direct shear wave would be largest near the Pacific coast, and decrease farther inland where ray paths arrive with a small (more vertical) incidence angle. As we noted earlier, the $S \times P$ and $S \times S$ phase in the data of Shot 21 (Figs 2a and 9) show the opposite variation with distance from the Pacific coast, with high $S \times S$ amplitudes inland, and high $S \times P$ amplitudes near the Pacific coast. The large-scale (0–60 km in Fig. 9) amplitude variation along the refraction line can be explained by a difference in reflection angles for $S \times P$ and $S \times S$ wave paths. The short-wavelength $S \times P$ and $S \times S$ amplitude variations observed along the array may represent variations in small-scale structure along the surface of the slab.

Using the ray trajectories of the slab reflections obtained with the traveltime analysis (Fig. 3), we can correct the reflection amplitudes for geometrical spreading and polarization angle. The ray geometry (Fig. 9b) does not predict large lateral differences in geometrical spreading for $S \times P$ and $S \times S$. On the other hand, the near-vertical approach of the ray paths toward the instruments at the Earth's surface has great implications for the true amplitude of the $S \times P$ and $S \times S$ phases. Due to the near-vertical incidence of the upward travelling wave paths, the orientation of these sensors is much more favourable to incoming $S \times P$ than to the $S \times S$ phase. Although $S \times S$ amplitudes were observed to be only slightly larger than $S \times P$ amplitudes in our data (Fig. 9c), we estimate that the true amplitude of the observed $S \times S$ waves was roughly four times larger than the amplitude of $S \times P$, although this amplitude ratio may have a large uncertainty. The polarization of high-frequency compressional and shear waves can locally deviate from the expected direction of particle motion by as much as 20° due to scattering from km-scale heterogeneities the crust (Menke & Lerner-Lam 1991). We therefore assume that a larger component of the $S \times P$ arrivals was recorded on the geophones than what we may assume from our ray geometry.

We estimate the $S \times P$ and $S \times S$ reflection amplitudes for all arrivals at the slab–mantle interface between distances of 28 and 45 km from the Pacific coast by stacking the frequency-dependent reflection amplitudes in 1-km-wide overlapping bins (Fig. 10). Our data analysis shows that both the $S \times P$ and $S \times S$ amplitudes increase strongly with frequency between 10 and 20 Hz. We do not see a variation in this basic character of the spectral amplitude with the angle of incidence at the plate interface, which increases steadily from 18° to 36° in the seaward direction. In the next section, we compare the calculated seismic response of velocity models of the plate interface with the reflection coefficient measured at 34 km (Fig. 10), where the angle of incidence is 28°. We will also verify whether the calculated $S \times P$ and $S \times S$ reflection amplitudes vary much between incidence angles 22° and 32°.

4.2 Reflectivity

Our analysis of the $S \times P$, $S \times S$, P_g and S_g phases of Shot 21 suggests a strong increase in the S–P and S–S reflection coefficients with frequency at the plate interface beneath the forearc of central Costa Rica. Assuming a shear wave speed V_s of 4.0 km s^{-1} in the forearc mantle, a 10 Hz wave impinging on the slab surface has a wavelength of approximately 400 m, whereas a 20 Hz wave has a wavelength of just 200 m. To get significantly different reflection amplitudes at these two frequencies, the plate interface must exhibit strong variations in seismic structure over distances that are just a fraction of the corresponding wavelengths. However, we do not anticipate that this reflector is the result of a juxtaposition of two plates with very different physical properties. The seismic velocities of the mantle wedge corner of central Costa Rica and the subducting oceanic crust are quite similar (Ye *et al.* 1996; Husen *et al.* 2003;
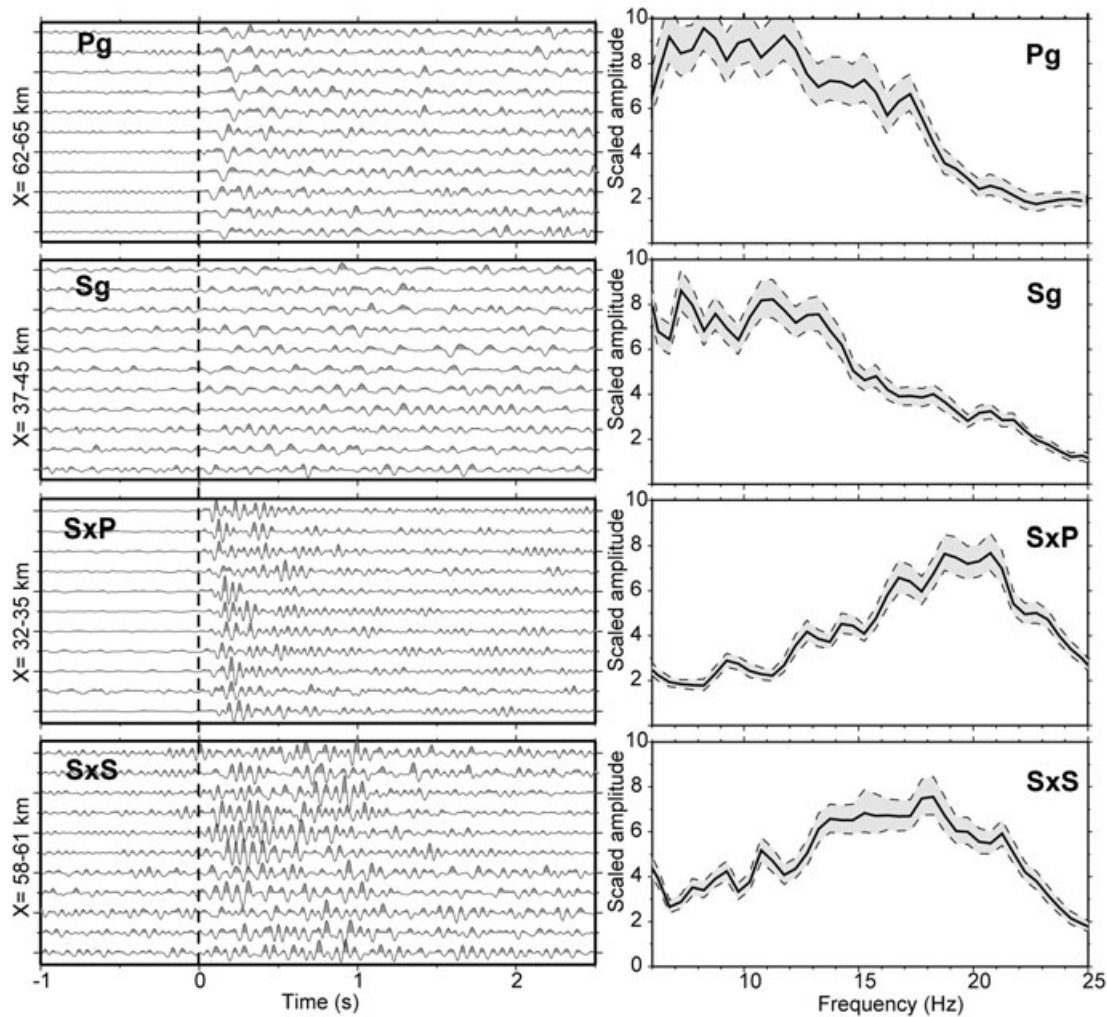
Figure 8. Time-series for the observed seismic phases P_g, S_g, $S{\times}P$ and $S{\times}S$ from Shot 21 (left) and their corresponding amplitude spectra (right). Distances from the Pacific coast at which these time-series were recorded are indicated on the left. Time on the horizontal axis is relative to the arrival of the seismic phases, which is marked by the vertical dashed line. All seismic amplitudes are scaled, such that the four phases appear approximately equal in magnitude. The grey area surrounding the spectrum (right) indicates a confidence level of one standard deviation.

DeShon & Schwartz 2004; Arroyo *et al.* 2009), so the reflections must be caused by anomalous structure within the shear zone itself. We therefore investigate whether a thin weak layer, or a series of weak layers, between the two bounding tectonic plates can explain our observations from Shot 21.

Our ray diagram (Fig. 9) shows that we expect the reflectivity of the plate interface to be fairly consistent over a distance of roughly 20 km, whereas we expect fine structure over distances less than 100 m across this boundary. The frequency-dependent reflection and transmission coefficients for plane waves in an 1-D medium with strongly varying properties can be calculated by using propagator matrices (Haskell 1962; Aki & Richards 2002). A simplified model for the shear zone may be composed of one or several thin, homogeneous layers. For each of these layers we specify V_p, V_s and mass density ρ, where we derive ρ from V_p following an empirical relationship (Brocher 2005). As we explained, we assume that the slab–mantle interface lies between a 15% serpentinized mantle wedge and metamorphosed oceanic crust. In all of our calculations, we assume a V_p of 7.2 km s^{-1} and a V_s of 4.0 km s^{-1} for both half spaces. We will obtain significant reflection coefficients (not much smaller than 1.0) if either V_p or V_s inside the shear zone is very different from the seismic velocities of the wall rock. The

most realistic scenario is that V_s is much smaller than 4.0 km s^{-1}, which could be the result of high fluid pressures at the slab–mantle interface (Christensen 1984).

In our first test, we verify whether a single 5-m-thick weak layer at the plate interface can preferentially reflect seismic waves of high frequency. We calculate the $S{\times}P$ and $S{\times}S$ reflection coefficients for a range of V_s and frequency at an incidence angle of $28°$. Both the $S{\times}P$ and $S{\times}S$ reflection coefficients increase with frequency and decrease with shear velocity in the shear zone layer, although $S{\times}S$ coefficients are consistently larger than $S{\times}P$ coefficients (Fig. 11). A similar difference between $S{\times}S$ and $S{\times}P$ amplitudes was apparent in the data from Shot 21 (Fig. 10). To make a direct comparison between the modelling results and our data from Shot 21, we select the reflection coefficients for $V_s = 1.0$, 2.0 and 3.0 km s^{-1} (horizontal lines in Fig. 11). The single-layer model can qualitatively reproduce the strengthening of reflection coefficients with frequency (Fig. 12a). However, the slopes of the frequency spectra from Shot 21 are too steep to be matched by this model, regardless of the V_s that is used inside the shear zone. For example, if the shear velocity is as low as 1.0 km s^{-1} in a 5-m-thick layer, the reflection coefficients for $S{\times}P$ and $S{\times}S$ at 20 Hz will be 0.17 and 0.48, respectively (Fig. 12a). These reflection coefficients are
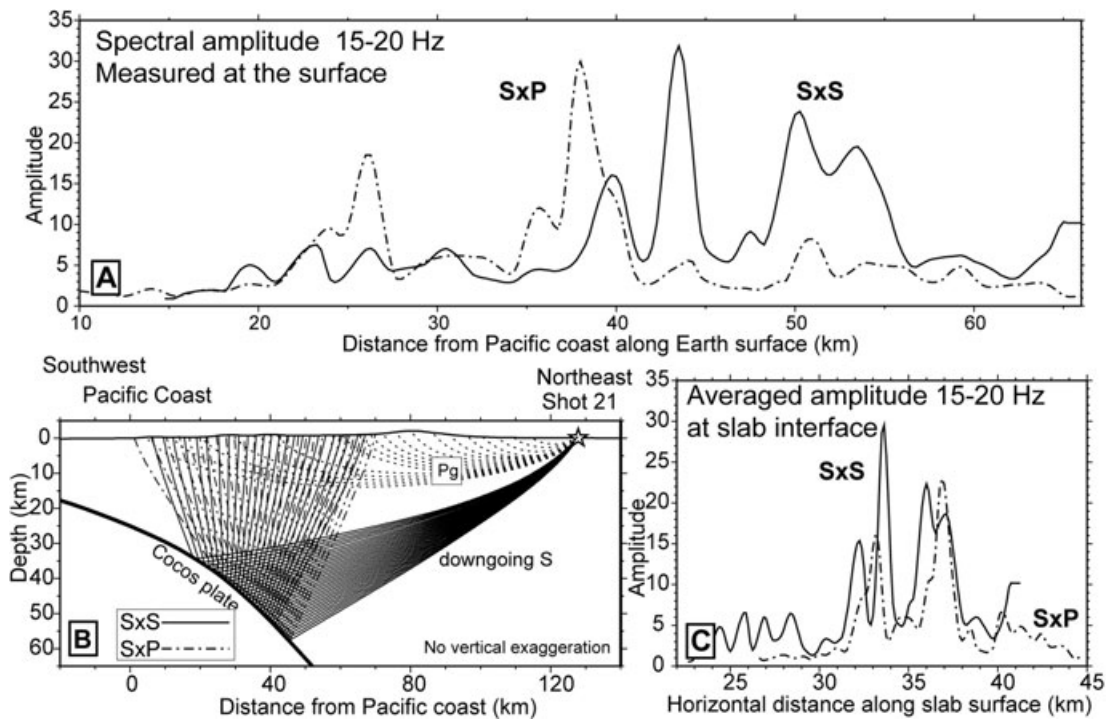
Figure 9. Projection of observed reflection spectra $S \times P$ and $S \times S$ from the Earth's surface onto the slab–mantle interface (Syracuse & Abers 2006) along ray paths. The compression of lateral offset from 55 km at the Earth's surface (a) to 25 km at the slab surface (c) is in part due to the convex shape of the downgoing plate.

large and increase by nearly a factor of 2 between 12 and 20 Hz, but this increase is less than the observed fourfold increase in this frequency band.

In a second test, we amplify the increase of reflection coefficients with frequency by assuming a series of 10 5-m-thick shear zones, spaced 45 m apart. This is a simplified model of a splayed fault system, where the fault strands are approximately parallel to the general trend of the megashear. As in our first test, we probe a range of seismic frequencies and V_s for the shear zones. The two bounding plates and layers of wall rock within the megashear are again all assumed to have a constant V_p of 7.2 km s^{-1} and constant V_s of 4.0 km s^{-1}. The calculated reflection coefficients for these 10-layer models show a strong increase in the reflection coefficients with decreasing V_s inside the shear zones and increasing frequency (Fig. 11b). A comparison of these modelling results for $V_s = 1.0, 2.0$ and 3.0 km s^{-1} inside the shear zones shows that they all predict an increase of the S–S and S–P reflection coefficients with frequency, but reflection coefficients for $V_s = 1.0$ km s^{-1} are much larger than for $V_s = 3.0$ km s^{-1}. The data fit of the 10-layer model (Fig. 12b) is much better than that of the single-layer model (Fig. 12a), but the choice of the best shear velocity V_s inside the shear zones of the multilayer model may require a closer inspection of the data.

The reflection amplitudes of Shot 21 (Fig. 2b) give an indication of the magnitude of the V_s anomaly represented by shear zones at the slab interface. The amplitude of the $S \times S$ and $S \times P$ phases are much larger than those of S_g and P_g, which can in part be explained by relatively small amounts of geometrical spreading for these reflections (Fig. 3). To observe these slab phases, it is also essential that the $S \times P$ and $S \times S$ reflection coefficients are not an order of magnitude smaller than 1.0. Our modelling shows that the $S \times S$ reflection coefficient is 0.9 at 20 Hz for $V_s = 1.0$ km s^{-1} (Fig. 12b), which is clearly large enough. In contrast, the same $S \times S$ coefficient is only 0.2 if $V_s = 2.0$ km s^{-1}, and it is smaller than

0.05 if $V_s = 3.0$ km s^{-1}. A second constraint on V_s inside the fault zones is the relative strength of $S \times P$ and $S \times S$ amplitudes. If $V_s = 1.0$ km s^{-1}, we find no clear difference in the data fit of $S \times P$ and $S \times S$ (Fig. 12b). On the other hand, if $V_s = 2.0$ or 3.0 km s^{-1}, the $S \times P$ coefficients are consistently higher than the best-fitting data curve, whereas the $S \times S$ coefficients fall below the scaled amplitude spectrum. These results suggest that models where the shear zones have a V_s of 2.0 or 3.0 km s^{-1} will underestimate the strength of $S \times S$ relative to $S \times P$, so we prefer a V_s as low as 1.0 km s^{-1} inside the 5-m-thick shear zones.

In a third calculation (Fig. 13), we verify whether changes in the angle of incidence between 22° and 32° have a large impact on the distribution of $S \times P$ and $S \times S$ reflection coefficients over the same range of frequency and V_s. As in the first example, where the angle is 28°, the reflection coefficients increase steadily with frequency, and $S \times S$ is significantly larger than $S \times P$. However, we see a gradual increase in the size of $S \times P$ reflection coefficients with angle of incidence, and a coincident decrease in the $S \times S$ reflection coefficients. This small trend was not observed in the data (Fig. 10). We cannot see a general trend in the variation of reflection amplitudes with angle of incidence, because these amplitudes vary on a much shorter wavelength (~2 km), presumably due to variations in structure along the slab surface.

A significant complication in the interpretation of $S \times P$ and $S \times S$ as slab reflections from Shot 21 is the absence of slab reflections from the incoming compressional (P) wave. A P wave can convert as a compressional ($P \times P$) and a shear ($P \times S$) wave at the slab–mantle interface. Our seismic velocity model of the upper 60 km of the subduction zone (Fig. 3c) would predict $P \times P$ and $P \times S$ phases from Shot 21 to arrive near the Pacific coast after the P_g phase, and before the $S \times P$ phase (Fig. 2a), but neither $P \times S$ or $P \times P$ were recorded. The absence of a $P \times P$ arrival from Shot 21 would seem consistent with the small reflection coefficient of this phase (Fig. 14). The
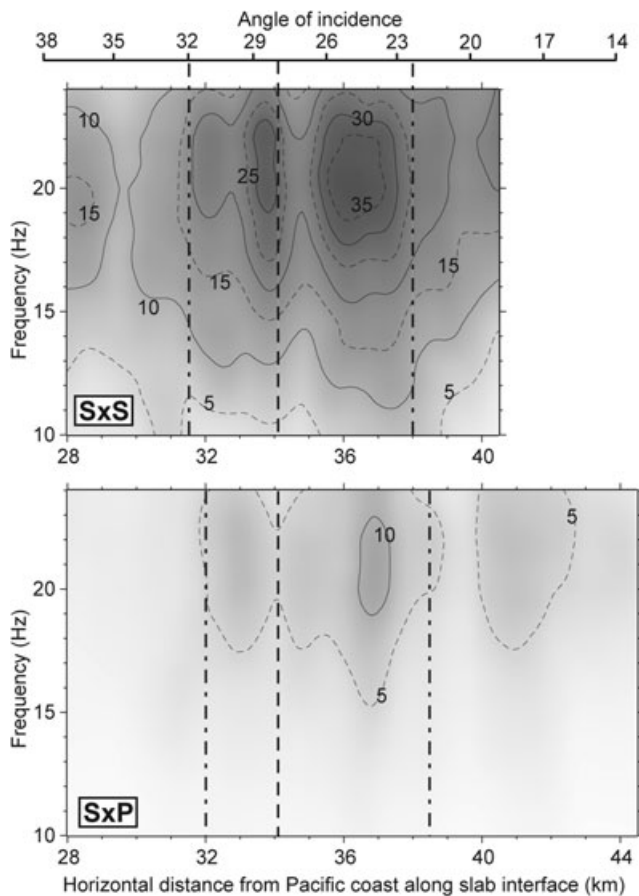
Figure 10. Reflection amplitude of Shot 21 wide-angle reflections $S{\times}P$ and $S{\times}S$. The spectral amplitudes are plotted as a function of horizontal distance along the slab interface and frequency. The vertical dashed line marks the spectrum at 34 km on the slab surface, where the angle of incidence of shear waves is 28°. The two dash-dotted lines mark the location where the angle of incidence is 32° and 22°. We use these particular incidence angles and spectra to compare with modelling results.

calculated $P{\times}P$ reflection coefficients are small because the difference in compressional velocity between weak (6.8 km s^{-1}) strong (7.2 km s^{-1}) layers in the reflectivity model of the slab–mantle interface is modest (6%). However, due to large (>100%) shear wave contrasts in this model of the slab–mantle interface (Fig. 12), the $P{\times}S$ reflection coefficients (Fig. 14) are similar to, and apparently even larger than, the calculated $S{\times}P$ coefficients (Fig. 11). The horizontal polarization of the $P{\times}S$ phase would not be favourable to the vertical-component record of Shot 21 (Fig. 2a), but the complete absence of the converted P wave in the data requires one of the following two explanations:

(1) Shot 21 emitted an unusually strong burst of shear wave energy at angles less than 40° from the vertical, which resulted in strong $S{\times}P$ and $S{\times}S$ arrival. In this scenario, the S_g wave from Shot 21 was weaker because it was emitted at shallower (larger) angles (Fig. 3). Although an unusually strong shear wave propagated at small angles from Shot 21, Shots 22, 23 and 24 did not radiate similar high-energy seismic waves toward the slab–mantle interface (Figs 2b–d).

(2) As discussed in Section 3.2, we were not able to find evidence of a second seismic source near the slab–mantle interface ~25 s after the detonation of Shot 21. Moreover, the variation of amplitude with distance of both the $S{\times}P$ and $S{\times}S$ phases along our profile

(Fig. 9) is inconsistent with that of a direct P and S waves from a second source in central Costa Rica. On the other hand, a separate seismic source for $S{\times}P$ and $S{\times}S$ provides a simple explanation for the absence of $P{\times}S$ for Shot 21, and other converted phases for Shots 22, 23 and 24.

4.3 Effect of attenuation (Q)

Our frequency analysis of the interpreted slab reflections $S{\times}P$ and $S{\times}S$ neglected the possible effect of intrinsic attenuation and scattering on the waveforms of all phases in the record of Shot 21. If attenuation significantly distorted the amplitude spectra of any of these three phases, our estimated frequency-dependent reflection coefficients (Fig. 12) are affected accordingly. Because intrinsic attenuation preferentially decreases the amplitude of high frequencies, it usually results in seismic amplitude spectra with steeper slopes at larger source–receiver offsets. However, the refractions from the TICOCAVA shots show a remarkable consistency in the shape of amplitude spectra. The spectra of Shots 21 and 22 (Fig. 15) show that the amplitudes may even increase slightly between 15 and 55 km offset. This characteristic may be explained by very low intrinsic attenuation (high Q), and trapping of high-frequency scattered waves in the upper crust (Dainty 1981; Davis & Clayton 2007). The consistency of the spectra of Shot 21 at different offsets (Fig. 15) gives us confidence that the P_g arrivals can be used to approximate the spectrum of the wave that impinges on the Cocos slab, but we must also consider the effect of attenuation on the $S{\times}P$ and $S{\times}S$ phases. At depths larger than a few kilometres, scattering may not be as important due to the high overburden pressure, so the $S{\times}P$ and $S{\times}S$ arrivals, which sample the entire crust and outer mantle wedge, may be more affected by intrinsic attenuation.

The best model for the attenuation structure in our study area comes from the TUCAN experiment. Rychert *et al.* (2008) show that Q_p and Q_s in the arc lithosphere are high, but a substantial low Q_p and Q_s anomaly (<100) resides in the mantle wedge beneath the volcanic front at depths between 70 and 100 km. This anomaly is too deep to be traversed by ray paths of the $S{\times}P$ and $S{\times}S$ arrivals (Fig. 16). Before we calculate the effect of attenuation on our analysis of Shot 21 using the TUCAN model, we note three reasons why we cannot determine it with much accuracy: (1) The TUCAN data provide constraints on the attenuation structure of the subduction zone ~140 km northwest of the TICOCAVA active-source seismic profile. We here assume that the attenuation structure does not vary along the strike of the arc, but the work of Rychert *et al.* (2008) suggests that Q_p and Q_s generally increase to the southeast. (2) The TUCAN data do not constrain attenuation in the top 15 km of the crust (Rychert *et al.* 2008). Based on the spectra of TICOCAVA shots (Fig. 15), we know that Q_p may be as high as 1000 in the upper crust. (3) Seismic attenuation is often assumed to be frequency dependent, particularly if it is caused by both an elasticity and seismic scattering (Toksöz *et al.* 1990). Seismic studies show that attenuation may be parameterized in the form $Q = Cf^\alpha$ both in the crust and in the mantle, but the frequency dependence α is generally larger in the crust (~0.65) than in the mantle (~0.27) (Stachnik *et al.* 2004).

With these provisions we use the TUCAN Q model (Rychert *et al.* 2008) to quantify the effect of seismic attenuation on our estimates of the $S{\times}P$ and $S{\times}S$ reflection coefficients (Fig. 12). First we integrate Q_p and Q_s, which are both calibrated at 1 Hz, along the ray paths from Shot 21 to obtain the path-averaged attenuation t_0^* (Fig. 15). The calculated t_0^* for the $S{\times}P$ and $S{\times}S$ arrivals from Shot
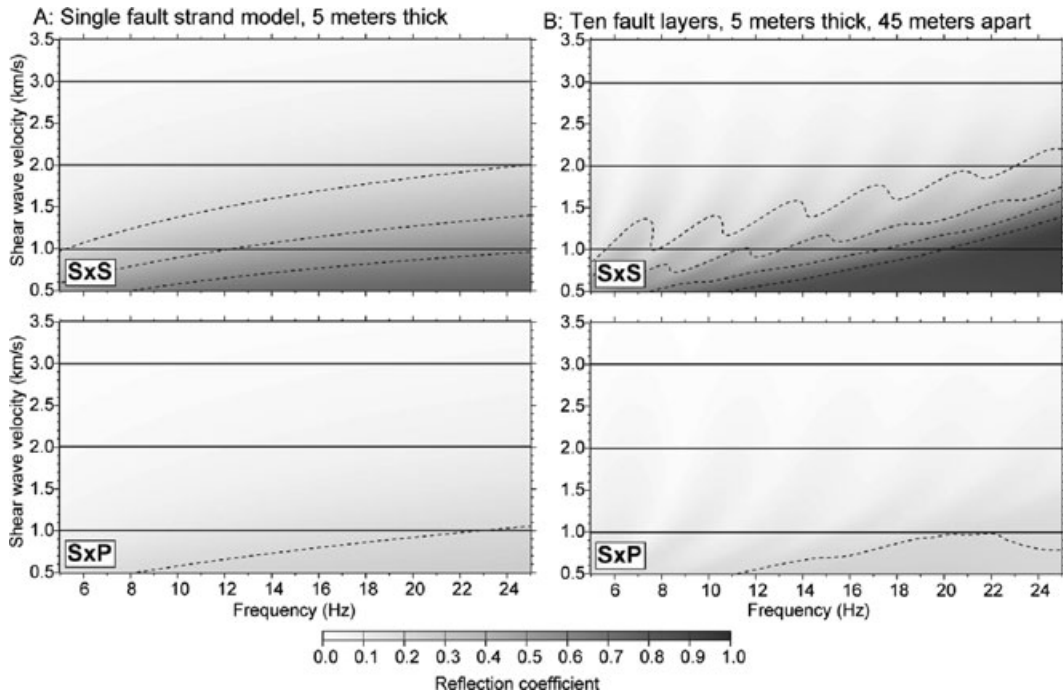
Figure 11. Calculation of $S{\times}P$ and $S{\times}S$ reflection coefficients for various V_s inside the faults zones and frequencies between 5 and 25 Hz. All reflection coefficients are contoured (dashed lines) at 0.2. We test two models: (a) a single weak zone of 5 m thickness and (b) a system of 10 5-m-thick fault zones that are spaced 45 m apart. The horizontal lines mark the reflection coefficient curves plotted in Fig. 12.
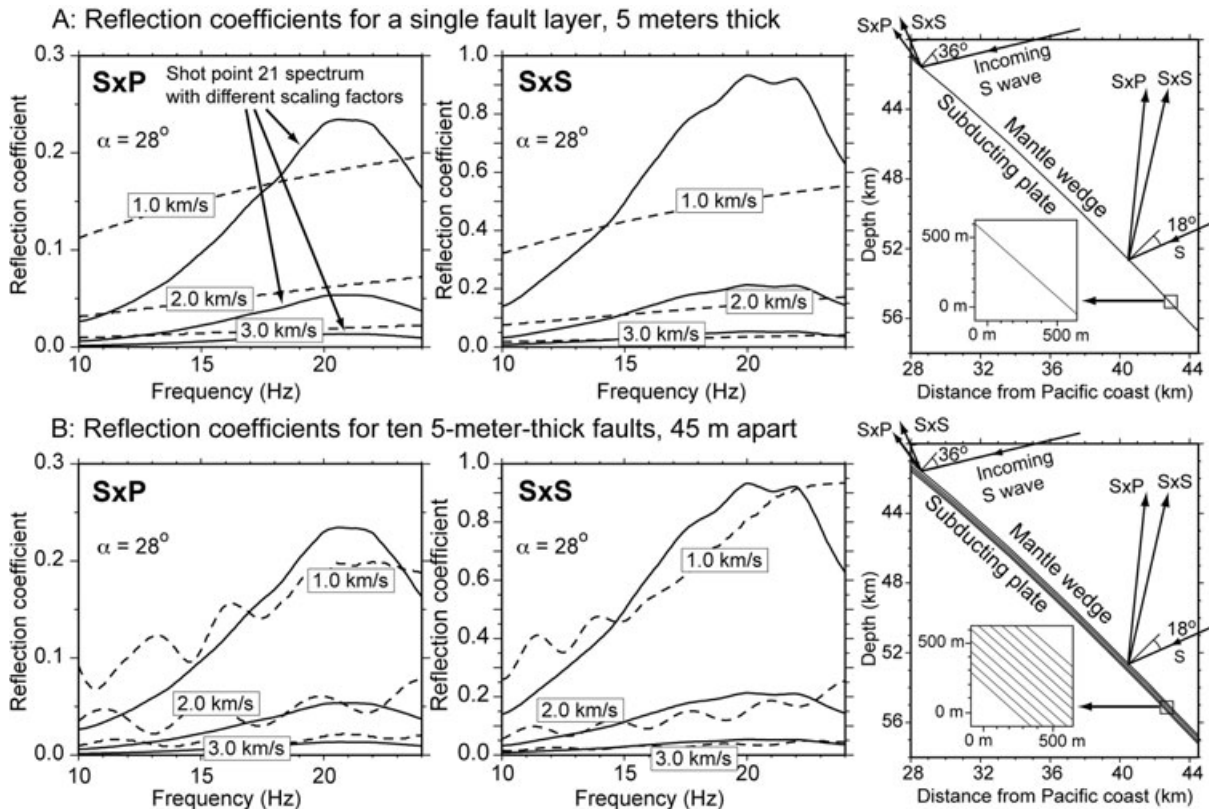

Figure 12. Variation of $S{\times}P$ and $S{\times}S$ reflection coefficient with frequency for a plane wave impinging on the slab surface at 28°. The reflection coefficients are calculated for (a) a single fault layer and (b) 10 thin fault layers. For each of these two models, we show the $S{\times}P$ and $S{\times}S$ response for the case that the shear wave velocity (V_s) inside the 5-m-thick fault zones is 1.0, 2.0 or 3.0 km s^{-1} (dashed curves). The $S{\times}P$ and $S{\times}S$ reflection amplitude measured from the refraction data (solid curve) is scaled to fit the reflection coefficient for each V_s. The roughness in the calculated reflection coefficients for the multilayer model (b) is due to reverberations within these layers. On the right side of the spectral plots we show a cartoon of the $S{\times}P$ and $S{\times}S$ ray paths together with the 1-D model for the plate boundary. The thin black lines in the insets represent the thin layers with low shear-wave velocity.
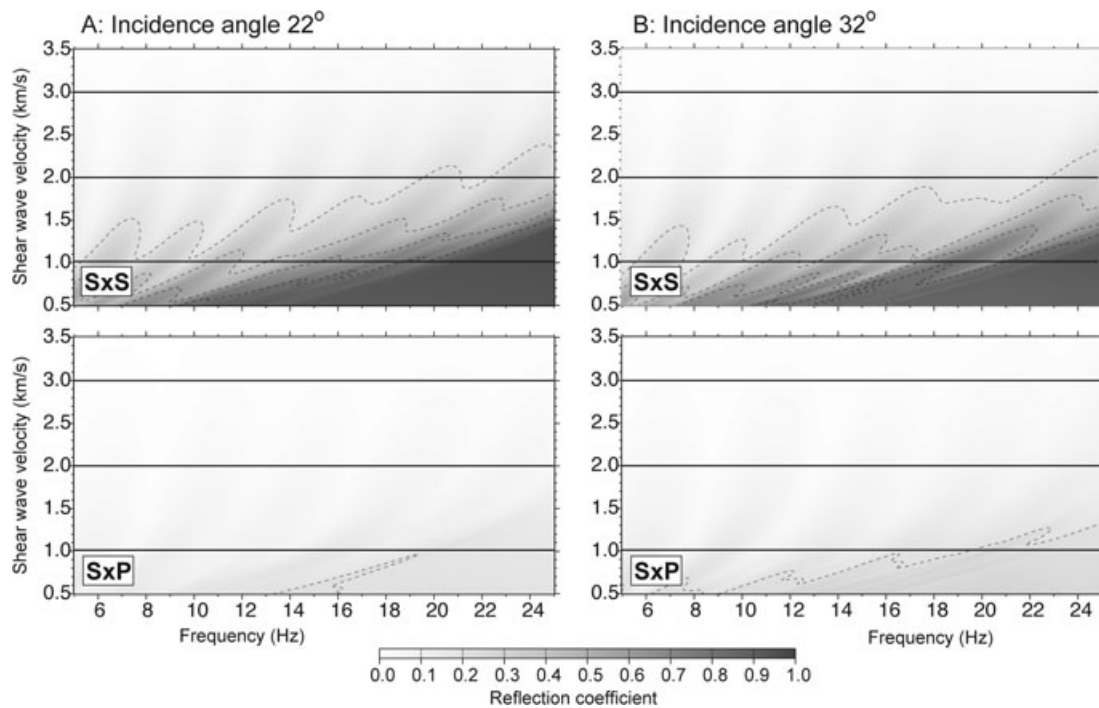
Figure 13. Calculation of $S \times P$ and $S \times S$ reflection coefficients at two different angles of incidence. Note that the amplitudes vary by only a small amount, but $S \times S$ decreases slightly with incidence angle, whereas $S \times P$ increases slightly with incidence angle.
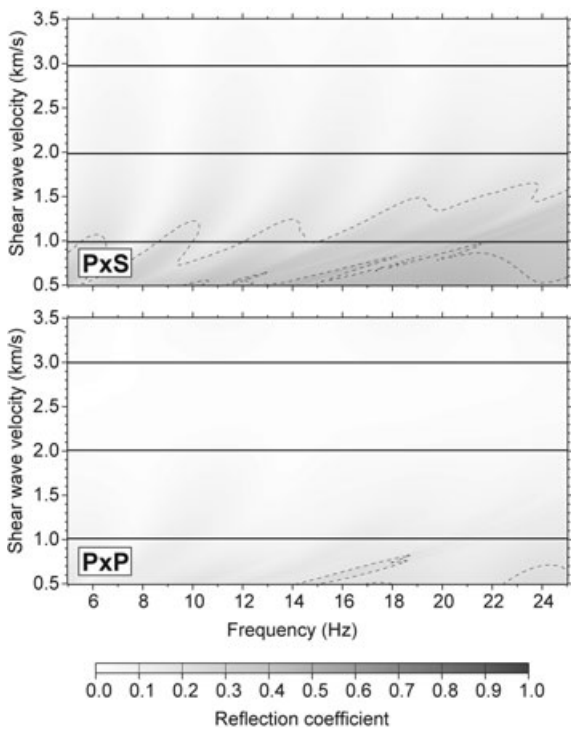

Figure 14. Calculation of $P \times P$ and $P \times S$ reflection coefficients for an angle of incidence of 28° and the same 10-layer model for a slab–mantle interface as in Fig. 12(b).

21 are fairly small (0.069–0.098 s), but not as small as the t_0^* for P_g arrivals (0.010–0.048 s). We expect a decrease in the spectral amplitude of all arrivals of the form $A(f t_0^*) = A_0(f) \exp(-\pi f^{1-\alpha} t_0^*)$, where $A_0(f)$ is the amplitude spectrum of the seismic arrival without attenuation. To obtain the reflection amplitude diagrams of Fig. 10,

we divided the $S \times S$ and $S \times P$ spectra by the spectrum of P_g arrivals with a t_0^* of 0.012 s. This t_0^* suggests a very small decay of P_g amplitude with frequency. The larger t_0^* of $S \times P$ and $S \times S$ imply that these slab reflections lost more of their high-frequency signal. As a result, our estimated reflection coefficients probably underestimated the amplitudes at higher frequencies. As we ignored attenuation, we found an increase in $S \times P$ and $S \times S$ amplitudes of about 7 between 10 and 20 Hz (Fig. 12), but the true increase of these amplitudes with frequency may have been even higher. In Fig. 17, we show to what degree reflection amplitudes for a given t_0^* and frequency may have decayed relative to the amplitude of the same t_0^* at 10 Hz. If we assume that $\alpha = 0.65$, as in many other crustal seismic studies (Stachnik *et al.* 2004), and $t_0^* = 0.080$, which is roughly the average for our observed $S \times P$ and $S \times S$ arrivals (Fig. 16), we find that the reflection arrival amplitude at 20 Hz is reduced to 0.75, relative to the amplitude at 10 Hz. Therefore, if our assumptions regarding the attenuation structure beneath the TICOCAVA transect are correct, we may have underestimated the increase of the $S \times S$ and $S \times P$ reflection coefficients with frequency between 10 and 20 Hz by roughly 25%. Given the uncertainties in the attenuation structure and other modelling assumptions in our analysis, this result does not alter the basic conclusions of our study. The discrepancy in frequency between seismic refractions and slab reflections from TICOCAVA Shot 21 is a remarkable observation that may be explained by a series of thin layers at the slab–mantle interface with unusually low shear-wave velocities.

5 DISCUSSION

5.1 Interpretation of $S \times P$ and $S \times S$

We have presented an unusual explosion seismology record from Shot 21 in the TICOCAVA study in central Costa Rica, in which we found crustal refractions P_g and S_g, with a dominant frequency
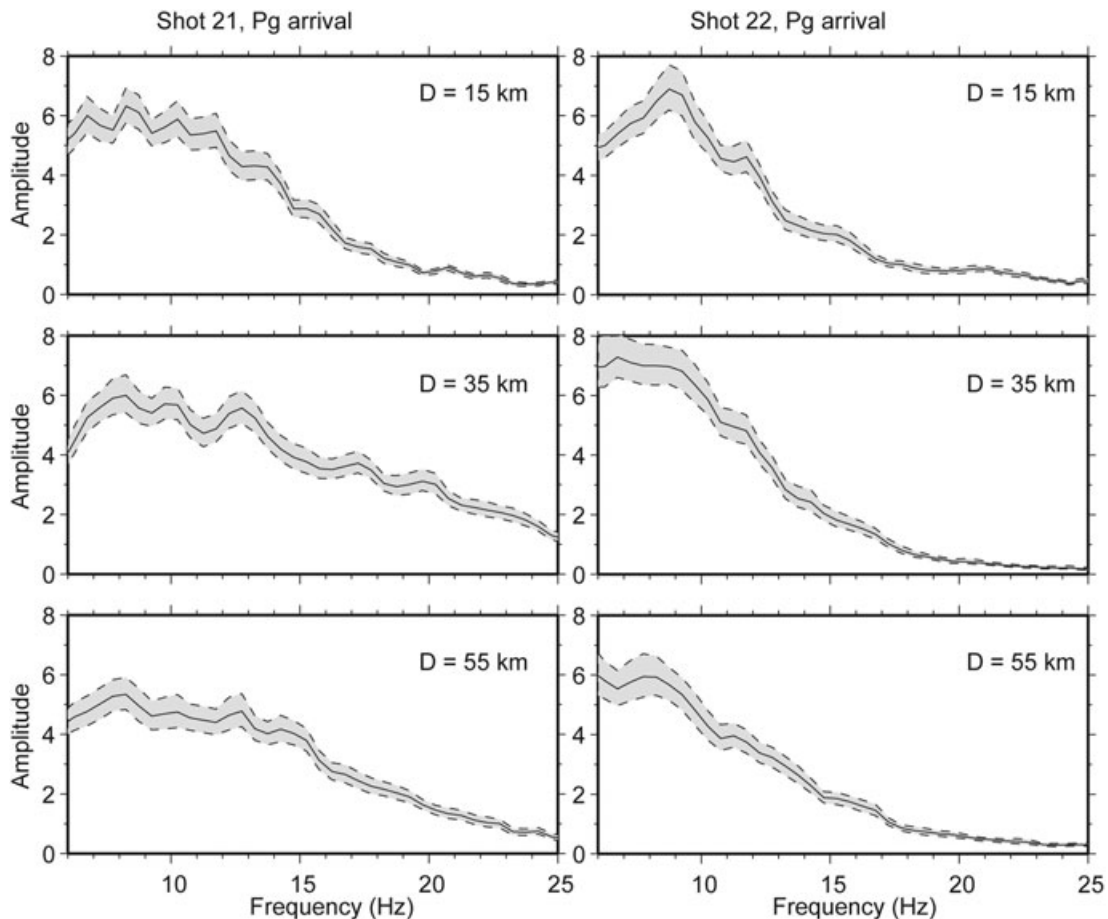
Figure 15. Spectra of P_g arrivals of Shots 21 and 22 at three different source-receiver offsets. The comparison shows that the spectrum of P_g does not vary much with recording distance. This observation is consistent with all other shots of the TICOCAVA study.

of ∼10 Hz, followed by two deep seismic phases ($S{\times}P$ and $S{\times}S$), which both have a dominant frequency of ∼20 Hz. The location of Shot 21 in the backarc suggests that we may have captured wide-angle reflections from the subducting Cocos slab across the forearc of the Costa Rican isthmus. In that case, the anomalous frequency of the $S{\times}P$ and $S{\times}S$ phases can give us new insight in the fine structure of the Cocos slab surface beneath the forearc mantle. A schematic overview of this analysis, including ray tracing, multitaper analysis, the calculation of spectral ratios and reflectivity modelling is shown in Fig. 18.

Our reflectivity model of the slab–mantle interface (Fig. 12) would also predict a strong $P{\times}S$ reflection (Fig. 14), which we did not observe in the record of Shot 21. Neither were $S{\times}P$ and $S{\times}S$ phases recorded for Shots 22, 23 and 24, the three other explosions in the backarc (Figs 2b–d). This interpretation of $S{\times}P$ and $S{\times}S$ would therefore imply that the two phases were converted at the slab interface from an unusually strong downward pulse of shear-wave energy from Shot 21. Alternatively, we consider the possibility that the $S{\times}P$ and $S{\times}S$ phases were produced by a small earthquake that happened just ∼25 s after Shot 21. There are a number of challenges to this second explanation for $S{\times}P$ and $S{\times}S$:

(1) The probability of recording an earthquake with an apparent source location and origin time similar to the arrival of a seismic wave from Shot 21 at the Cocos slab is small. Our traveltime constraints show that the $S{\times}P$ and $S{\times}S$ waves did not come from Costa Rica's seismogenic zone offshore or near the Pacific coast (Fig. 4a).

However, the traveltimes alone do not rule out the possibility that these phases originated from a point source ∼40 km inland and roughly 52 km deep (Fig. 4b), a location that we named Q (Fig. 5). The subducting oceanic lithosphere exhibits diffuse seismicity at this depth (Husen *et al.* 2003). A small earthquake located northwest or southeast (Q_{NW} and Q_{SE} in Fig. 5) of our refraction profile would have to be at a shallower depth in the forearc crust to be consistent with the $S{\times}P$ and $S{\times}S$ traveltimes. The forearc crust in our study area experiences relatively few earthquakes (Protti *et al.* 1995), so these shallower locations adjacent to our refraction line are less likely as a source for $S{\times}P$ and $S{\times}S$ than location Q.

(2) Seismic stations throughout central Costa Rica recorded turning waves (P_g and S_g) from Shot 21 and small local earthquakes (Figs 6 and 7), but the $S{\times}P$ and $S{\times}S$ phases were only observed in the forearc. A ray diagram (Fig. 4b) shows that seismic waves from location Q would travel a relatively short distance to seismic stations in the arc and backarc region, but the high-frequency phases were not observed here. An interpretation of the $S{\times}P$ and $S{\times}S$ as specular reflections from the Cocos slab, with Shot 21 as their source in the backarc, provides an explanation for the absence of these phases farther to the northeast.

(3) The spectra of $S{\times}P$ and $S{\times}S$ (Fig. 8) are unlike those of small earthquakes in central Costa Rica (Fig. 7). According to dislocation models, the magnitude of an earthquake and its frequency content both scale with the size of the rupture surface (Aki 1967). The ∼7 s delay between the $S{\times}P$ and $S{\times}S$ phases requires that they travelled separately over a distance of approximately 50–60 km.
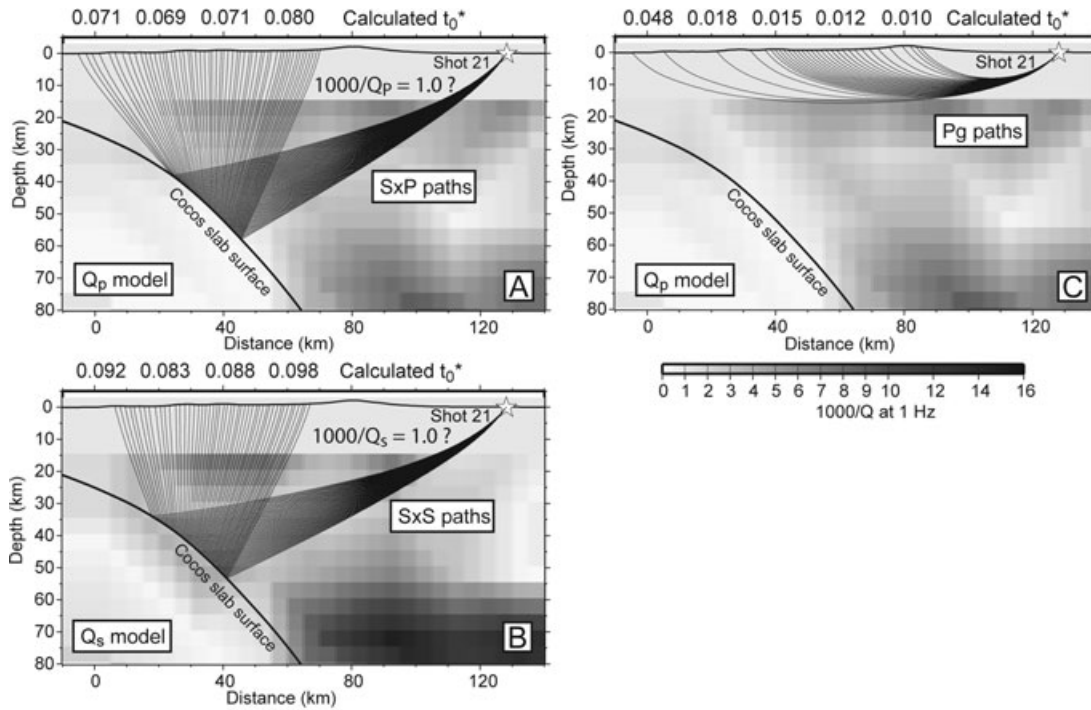
Figure 16. Calculated effect of attenuation on Shot 21 P_g, $S \times P$ and $S \times S$ phases, and their effect on inferred $S \times P$ and $S \times S$ reflection coefficients. We used the attenuation model for Q_p and Q_s from the TUCAN experiment (Rychert *et al.* 2008) (see Fig. 5, for location), which is calibrated at 1 Hz, to calculate t_0^* for (a) $S \times P$, (b) $S \times S$ and (c) P_g arrivals. The TUCAN attenuation model does not cover the top 15 km of the crust. Based on the fact that TICOCAVA P_g spectra show little change with source–receiver offset (Fig. 15), we assume that intrinsic compressional (Q_p) and shear (Q_s) attenuation in the upper crust may be as high as 1000. As a result, t_0^* may be as low as 0.012 for P_g, whereas the TUCAN Q model predicts a t_0^* of 0.069–0.080 for $S \times P$ and 0.083–0.098 for $S \times S$.
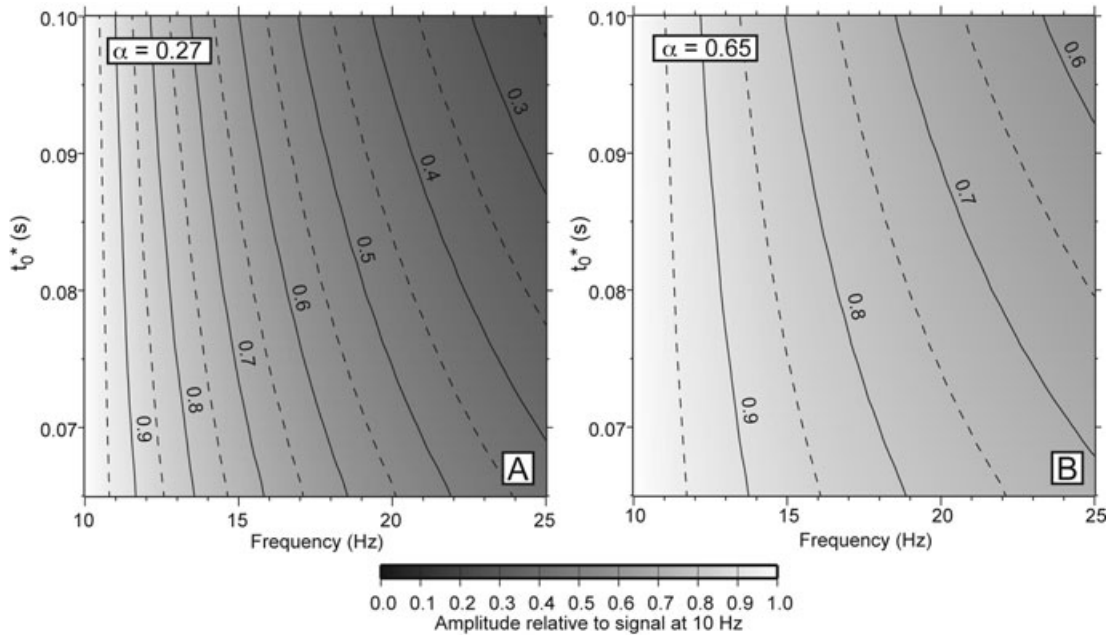

Figure 17. Variation in seismic amplitudes due to attenuation calculated over a range of frequencies and t_0^*. Because we want to compare different frequencies for a fixed t_0^*, we have normalized all results such that the amplitude at 10 Hz is 1.0. Following previous work on seismic attenuation, we assume that Q is proportional to f^α, where α is determined empirically. (a) In the TUCAN experiment (Rychert *et al.* 2008) and other studies of the mantle wedge (Stachnik *et al.* 2004), Q appears to increase slowly with frequency ($\alpha = 0.27$), which leads to a steady decrease of seismic amplitudes with frequency. (b) We assume that the TUCAN model (Rychert *et al.* 2008) (Fig. 15) makes an accurate prediction of Q around 10 Hz, because the spectral slopes t^* were measured between 1 and 20 Hz. However, many seismic attenuation studies assume a higher α to describe the frequency dependence of Q in the crust (Stachnik *et al.* 2004; Atkinson 1995; Li *et al.* 2006). We therefore parameterize Q with $\alpha = 0.65$ for frequencies between 10 and 25 Hz. The result is a slower decay of seismic amplitudes with frequency than in (a).
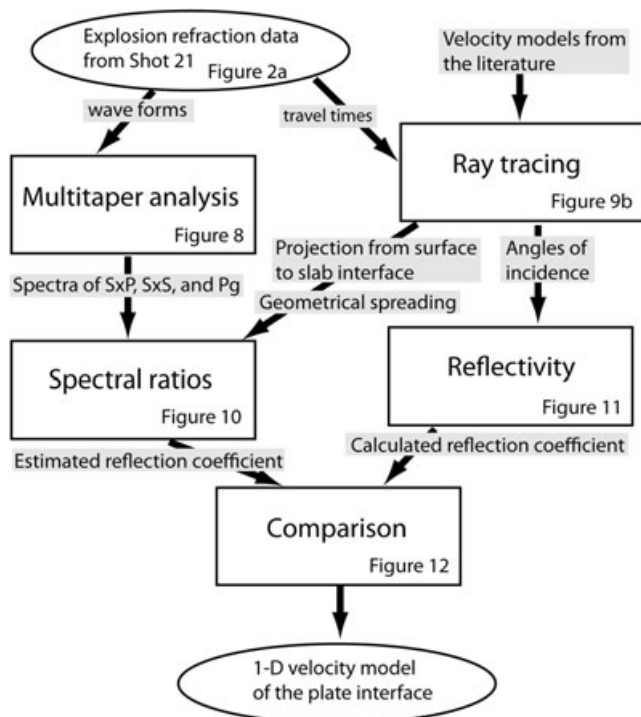
Figure 18. Flow diagram for the data analysis and modelling of reflection amplitudes.

The amplitude of these phases (Fig. 2) is nonetheless high, so they must have originated from an event of significant size. On the other hand, the ~20 Hz dominant frequency, which in this context could be interpreted as the second corner frequency of an earthquake, requires that the rupture had a magnitude $M_w < 0$ (Aki 1967). Such a low magnitude would not be detectable. It is therefore difficult to reconcile the strong amplitude of the $S \times P$ and $S \times S$ phases with their high dominant frequency if the source of this event was an earthquake or similar dislocation event, as opposed to an explosive or implosive event.

(4) The variation in amplitudes of the $S \times P$ and $S \times S$ phases with distance along our vertical-component instrument array (Fig. 2a) is difficult to reconcile with a point source at large depth in central Costa Rica. The $S \times P$ amplitudes are largest near the Pacific coast whereas $S \times S$ are largest inland (Fig. 9a), which is opposite of what we would expect if the observed lateral amplitude variations track the vertical component of direct P and S waves from a point source. Alternatively, if $S \times P$ and $S \times S$ are wide-angle reflections, the wider reflection angle of the $S \times P$ wave paths would explain the lateral offset of these two phases at the surface (Fig. 9b). The good correlation of $S \times P$ and $S \times S$ amplitude variations on the slab surface on length scales of a few kilometres suggests that they represent seismic structure at the plate interface (Fig. 9c).

We have not explored the nature of a possible second source that could have produced the $S \times P$ and $S \times S$ phases during Shot 21. As we mentioned, the high-frequency character of these arrivals suggests that they were not produced by a fault dislocation (Aki 1967). A volcanic origin must also be ruled out, because the traveltimes constrain the origin of such an event to the forearc of Costa Rica, roughly 50 km southwest of the volcanic arc (Fig. 5). If the $S \times P$ and $S \times S$ phases were indeed produced by a small earthquake in central Costa Rica, a key question is whether its mechanism is related to subduction of the Cocos slab. More observations of such

high-frequency seismic waves would be necessary to place this occurrence in a tectonic context.

5.2 Implications for slab interface structure

The models that we developed to explain $S \times P$ and $S \times S$ as high-frequency slab reflections of Shot 21 suggest that the shear-wave velocity at the plate interface is locally quite low (1–2 km s^{-1}), with low shear-strength material accumulated into banded layers with a thickness of roughly 5 m, spaced ~45 m apart. This modelling result does not depend strongly on the angle of incidence (Fig. 13), and it is also robust with respect to variations in the number of weak layers in the shear zone, or the distance between them. Each of the thin faults within a complex shear zone will preferentially reflect the higher frequencies of an incoming shear wave (Fig. 11a), and the aggregate effect for the plate boundary can be a reflection coefficient that is strongly dependent on frequency (Fig. 11b). We consider 2-D and 3-D models of the plate interface outside the scope of this paper, but small variations in the dip of the individual fault strands should not have a large effect on the cumulative reflection coefficients.

The suggested shear velocity of <2 km s^{-1} inside these fault zones is too low for known crustal or mantle rock properties at hydrostatic pressures (Hacker *et al.* 2003). On the other hand, if fluid pressure in the pore space at the plate interface approaches the lithostatic pressure, V_s will decrease much more rapidly than V_p (Christensen 1984). We envision that fluid release from the subducting slab, combined with low permeability, are responsible for a V_p/V_s ratio as high as 6 at the slab–mantle interface in Central Costa Rica. Offshore Costa Rica, sediment compaction at the base of the accretionary wedge similarly leads to a very high V_p/V_s ratio of 2.8 to 5.2 (Schnabel *et al.* 2007). These results suggest that the Cocos Plate interface is an important conduit for fluids that are released from the subducting slab. Limited permeability in the adjacent wall rock (Mibe *et al.* 1999) can lead to overpressures near the plate interface (Wada *et al.* 2008), which would explain the high V_p/V_s ratios (Christensen 1984).

Our model for the slab–mantle interface (Fig. 12b) could represent a ~500-m-wide system of roughly 5 m thick, anastomosing fault zones under high pore pressure. The presence of such a fault system is consistent with current interpretations of strain localization in a brittle–ductile transition (Mancktelow & Pennacchioni 2005). New faults can form as hydrofractures in the upper or lower plate near the subduction thrust, after which they develop into broader ductile shear zones with increasing strain and fluid–rock interaction. Such a fault system would form a mixing zone between the subducting oceanic lithosphere and the overlying mantle wedge (Bebout 2007). At a tectonically eroding margin such as in Costa Rica (Vannucchi *et al.* 2003), high fluid pressures at the plate interface may weaken and disintegrate rocks from the forearc mantle, a mechanism that von Huene *et al.* (2004) already proposed for the shallower subduction zone. The ability of this dynamic system of shear zones to maintain weak tectonic coupling between the two plates, even in the presence of large structural heterogeneities on the slab surface, may be required to sustain subduction over tens of millions of years (De Franco *et al.* 2008).

The depths of 35–55 km over which we infer high observed high seismic reflection coefficients coincides well with the depth range over which we anticipate a large release of aqueous fluids due to the metamorphic transition from blueschist to eclogite facies in subducting oceanic crust of the Cocos Plate (Husen *et al.*

2003; Spandler *et al.* 2003; Bebout 2007). Another source of the hydrous fluids that could be responsible for high seismic impedance at the slab interface beneath the forearc is the breakdown of serpentinites from the downgoing oceanic mantle (Ranero *et al.* 2003; Grevemeyer *et al.* 2007; Ivandic *et al.* 2008). Geodynamic models of the subduction zone in Central Costa Rica predict that the surface of the oceanic slab undergoes a rapid increase in temperature from approximately 300 °C to 700 °C as it descends into the mantle wedge (Peacock *et al.* 2005). Some of these fluids will infiltrate the mantle wedge corner despite the low permeability (Mibe *et al.* 1999), but a considerable portion of the subducting H_2O will drain back toward the accretionary prism (Zhu *et al.* 2009; Arroyo *et al.* 2009), where it may be released through fractures and cold seeps (Klaucke *et al.* 2008; Ranero *et al.* 2008). Chemically bound water stored deeper in the subducting lithosphere may be insulated from the hotter mantle wedge during subduction (Peacock *et al.* 2005). This portion of the H_2O budget will be released at greater depths, where it can contribute to arc magmatism (Schmidt & Poli 1998; Rüpke *et al.* 2004), or it may be recycled into the lower mantle (Hacker 2008).

5.3 Implications for seismogenesis

The portion of the Cocos slab surface beneath Costa Rica where we infer a zone of high V_p/V_s ratios covers distances of 25–40 km from the Pacific coast. The presence of fluids at the plate boundary would reduce the amount of tectonic coupling, and we assume that present-day plate motion here is accommodated by steady-state creep and transient slip on slab-parallel shear zones under high fluid pressure (Shelly *et al.* 2006; Liu & Rice 2007). We may have observed the anomalously weak plate interface, manifest as anomalous seismic reflectivity, at depths as shallow as 35 km. This depth is roughly the same as the lower limit of the seismogenic zone in this region (DeShon *et al.* 2003).

Perhaps the most applicable record of the seismogenic properties of the subduction zone in central Costa Rica comes from the seismicity before and after the 1990 earthquake in the Gulf of Nicoya (Protti *et al.* 1995), since this event ruptured an asperity just up-dip of our study area (Fig. 1). The distribution of foreshocks and aftershocks from this large earthquake shows a history of loading and relaxation of the plate boundary offshore, but it did not involve the portion of the Cocos Plate interface where we infer high V_p/V_s ratios (Fig. 1). The presence of hydrous fluids, released from the subducting Cocos Plate during prograde metamorphic reactions, may have prevented the accumulation of large stresses at the shear zone prior to the 1990 earthquake.

6 CONCLUSIONS

During an explosion seismology study in central Costa Rica, we recorded deep seismic phases that we interpret to be reflections from the subducting Cocos Plate beneath the forearc mantle. The frequency of these reflections is very high (~20 Hz) compared to the average frequency of turning waves in this experiment (~10 Hz). We explain this discrepancy with a seismic velocity model for the plate boundary that preferentially reflects the higher seismic frequencies. This model consists of 10 5-m-thick layers with a shear wave velocity V_s as low as 1.0 km s^{-1}. These thin layers may represent a system of fault zones under high pore pressure. The 35–55 km depth interval in which we inferred this reflective portion of the plate boundary coincides with the likely depth range

of dehydration reactions in the subducting oceanic lithosphere, and it lies downdip of the seismogenic zone offshore central Costa Rica. These correlations suggest a strong relationship between shearing and deformation between the two plates, the availability of water from dehydration reactions in the oceanic lithosphere, and the rheology of the shear zone.

REFERENCES

Abers, G.A., Plank, T. & Hacker, B.R., 2003. The wet Nicaraguan slab, *Geophys. Res. Lett.,* **30,** 1098, doi:10.1029/2002GL015649.

Adamek, S., Tajima, F. & Wiens, D.A., 1987. Seismic rupture associated with subduction of the Cocos Ridge, *Tectonics,* **6,** 757–774.

Aki, K., 1967. Scaling of seismic spectrum, *J. geophys. Res.,* **72,** 1217–1231.

Aki, K. & Richards, P.G., 2002. *Quantitative Seismology,* University Science Books, Sausalito, CA.

Alvarado, G.E., Denyer, P. & Sinton, C.W., 1997. The 89 Ma Tortugal komatiitic suite, Costa Rica: implications for a common geological origin of the Caribbean and Eastern Pacific region from a mantle plume, *Geology,* **25,** 439–442, doi:10.1130/0091-7613(1997)025<0439:TMTKSC>2.3.CO;2.

Arroyo, I.G., Husen, S., Flueh, E.R., Gossler, J., Kissling, E. & Alvarado, G.E., 2009. Three-dimensional P-wave velocity structure on the shallow part of the central Costa Rican Pacific margin from local earthquake tomography using off- and onshore networks, *Geophys. J. Int.,* **179,** 827–849, doi:10.1111/j.1365-246X.2009.04342.x.

Atkinson, G.M., 1995. Attenuation and source parameters of earthquakes in the Cascadia region, *Bull. seism. Soc. Am.,* **85,** 1327–1342.

Audet, P., Bostock, M.G., Christensen, N.I. & Peacock, S.M., 2009. Seismic evidence for overpressured subducted oceanic crust and megathrust fault sealing, *Nature,* **457,** 76–78, doi:10.1038/nature07650.

Barckhausen, U., Ranero, C.R., von Huene, R., Cande, S.C. & Roeser, H.A., 2001. Revised tectonic boundaries in the Cocos plate off Costa Rica: implications for the segmentation of the convergent margin and for plate tectonic models, *J. geophys. Res.,* **106,** 19 207–219 220, doi:10.1029/2001JB000238.

Barnicoat, A.C. & Cartwright, I., 1995. Focused fluid flow during subduction: oxygen isotope data from high-pressure ophiolites of the western Alps, *Earth planet. Sci. Lett.,* **132,** 53–61.

Bebout, G.E., 2007. Metamorphic chemical geodynamics of subduction zones, *Earth planet. Sci. Lett.,* **260,** 373–393.

Bilek, S.L. & Lithgow-Bertelloni, C., 2005. Stress changes in the Costa Rica subduction zone due to the 1999 Mw = 6.9 Quepos earthquake, *Earth planet. Sci. Lett.,* **230,** 97–112.

Bilek, S.L., Schwartz, S.Y. & DeShon, H.R., 2003. Control of seafloor roughness on earthquake rupture behavior, *Geology,* **31,** 455–458.

Brocher, T.M., 2005. Empirical relations between elastic wavespeeds and density, *Bull. seism. Soc. Am.,* **95,** 2081–2092.

Christensen, N.I., 1984. Pore pressure and oceanic crustal seismic structure, *Geophys. J. R. astr. Soc.,* **79,** 411–423.

Christensen, N.I., 2004. Serpentinites, peridotites, and seismology, *Int. Geol. Rev.,* **46,** 795–816, doi:10.2747/0020-6814.46.9.795.

Dainty, A.M., 1981. A scattering model to explain seismic Q observations in the lithosphere between 1 and 30 Hz, *Geophys. Res. Lett.,* **8,** 1126–1128.

Davis, P.M. & Clayton, R.W., 2007. Application of the telegraph model to coda Q variations in southern California, *J. geophys. Res.,* **112,** B09302, doi:10.1029/2006JB004542.

De Franco, R., Govers, R. & Wortel, R., 2008. Nature of the plate contact and subduction zones diversity, *Earth planet. Sci. Lett.,* **271,** 245–253.

DeMets, C., 2001. A new estimate for present-day Cocos-Caribbean plate motion: Implications for slip along the Central American volcanic arc, *Geophys. Res. Lett.,* **28,** 4043–4046.

DeShon, H.R. & Schwartz, S.Y., 2004. Evidence for serpentinization of the forearc mantle wedge along the Nicoya Peninsula, Costa Rica, *Geophys. Res. Lett.,* **31,** L21611, doi:10.1029/2004GL021179.

DeShon, H.R., Schwartz, S.Y., Bilek, S.L., Dorman, L.M., Gonzalez, V., Protti, M., Flueh, E. & Dixon, T.H., 2003. Seismogenic zone structure of the southern Middle America Trench, Costa Rica, *J. geophys. Res.,* **108,** 2491, doi:10.1029/2002JB002294.

DeShon, H.R. *et al.*, 2006. Seismogenic zone structure beneath the Nicoya Peninsula, Costa Rica, from three-dimensional local earthquake P- and S-wave tomography, *Geophys. J. Int.,* **164,** 109–124.

Ghosh, A., Newman, A.V., Thomas, A.M. & Farmer, G.T., 2008. Interface locking along the subduction megathrust from b-value mapping near Nicoya Peninsula, Costa Rica, *Geophys. Res. Lett.,* **35,** L01301, doi:10.1029/2007GL031617.

Grevemeyer, I., Ranero, C.R., Flueh, E.R., Kläschen, D. & Bialas, J., 2007. Passive and active seismological study of bending-related faulting and mantle serpentinization at the Middle America trench, *Earth planet. Sci. Lett.,* **258,** 528–542.

Hacker, B.R., 2008. H$_2$O subduction beyond arcs, *Geochem. Geophys. Geosyst.,* **9,** Q03001, doi:10.10292007GC001707.

Hacker, B.R., Abers, G.A. & Peacock, S.M., 2003. Subduction Factory 1. Theoretical mineralogy, densities, seismic wave speeds, and H$_2$O contents, *J. geophys. Res.,* **108,** 2029, doi:10.1029/2001JB001127.

Haskell, N., 1962. Crustal reflections of plane P and SV waves, *J. geophys. Res.,* **67,** 4751–4767.

Hauff, F., Hoernle, K., Schmincke, H.-U. & Werner, J., 1997. A Mid Cretaceous origin for the Galápagos hotspot: volcanological, petrological and geochemical evidence for Costa Rican oceanic crustal segments, *Geol. Rund.,* **86,** 141–155.

Hilairet, N., Reynard, B., Wang, Y., Daniel, I., Merkel, S., Nishiyama, N. & Petitgirard, S., 2007. High-pressure creep of serpentine, interseismic deformation, and initiation of subduction, *Science* **318,** 1910–1913.

Husen, S., Kissling, E. & Quintero, R., 2002. Tomographic evidence for a subducted seamount beneath the Gulf of Nicoya, Costa Rica: the cause of the 1990 Mw = 7.0 Gulf of Nicoya earthquake, *Geophys. Res. Lett.,* **29,** 1238, doi:10.1029/2001GL014045.

Husen, S., Quintero, R., Kissling, E. & Hacker, B., 2003. Subduction-zone structure and magmatic processes beneath Costa Rica constrained by local earthquake tomography and petrological modeling, *Geophys. J. Int.,* **155,** 11–32.

Hyndman, R.D. & Peacock, S.M., 2003. Serpentinization of the forearc mantle, *Earth planet. Sci. Lett.,* **212,** 417–432.

Ivandic, M., Grevemeyer, I., Berhorst, A., Flueh, E.R. & McIntosh, K., 2008. Impact of bending related faulting on the seismic properties of the incoming oceanic plate offshore of Nicaragua, *J. geophys. Res.,* **113,** B05410, doi:10.1029/2007JB005291.

Klaucke, I., Masson, D.G., Petersen, C.J., Weinrebe, W. & Ranero, C.R., 2008. Multifrequency geoacoustic imaging of fluid escape structures offshore Costa Rica: implications for the quantification of seep processes, *Geochem. Geophys. Geosyst.,* **9,** Q04010, doi:10.1029/2007GC001708.

Kodaira, S., Iidaka, T., Kato, A., Park, J.-O., Iwasaki, T. & Kaneda, Y., 2004. High pore fluid pressure may cause silent slip in the Nankai Trough, *Science,* **304,** 1295–1298.

LaFemina, P. *et al.*, 2009. Fore-arc motion and Cocos Ridge colli-

sion in Central America, *Geochem. Geophys. Geosyst.,* **10,** Q05S14, doi:10.1029/2008GC002181.

Li, Q., Wilcock, W.S.D., Pratt, T.L., Snelson, C.M. & Brocher, T.M., 2006. Seismic attenuation structure of the Seattle basin, Washington state, from explosive-source refraction data, *Bull. seism. Soc. Am.,* **96,** 553–571.

Liu, Y. & Rice, J.R., 2007. Spontaneous and triggered aseismic deformation transients in a subduction fault model, *J. geophys. Res.,* **112,** B09404, doi:10.1029/2007JB004930.

MacKenzie, L., Abers, G.A., Fischer, K.M., Syracuse, E.M., Protti, J.M., Gonzalez, V. & Strauch, W., 2008. Crustal structure along the southern Central American volcanic front, *Geochem. Geophys. Geosyst.,* **9,** Q08S09, doi:10.1029/2008GC001991.

MacMillan, I., Gans, P.B. & Alvarado, G., 2004. Middle Miocene to present plate tectonic history of the southern Central American volcanic arc, *Tectonophysics,* **392,** 325–348.

Mancktelow, N.S. & Pennacchioni, G., 2005. The control of precursor brittle fracture and fluid–rock interaction on the development of single and paired ductile shear zones, *J. Struct. Geol.,* **27,** 645–661, doi:10.1016/j.jsg.2004.12.001.

Manea, V. & Gurnis, M., 2007. Subduction zone evolution and low viscosity wedges and channels, *Earth planet. Sci. Lett.,* **264,** 22–45.

Mann, P., Rogers, R.D. & Gahagan, L., 2007. Overview of plate tectonic history and its unresolved tectonic problems, in *Central America – Geology, Resources, Hazards,* pp. 201–237, eds Bundschuh, J. & Alvarado, G., Taylor and Francis, London.

Menke, W. & Lerner-Lam, A., 1991. Observations of the transition from linear polarization to complex polarization in short-period compressional waves, *Bull. seism. Soc. Am.,* **81,** 611–621.

Mibe, K., Fujii, T. & Yasuda, A., 1999. Control of the location of the volcanic front in island arcs by aqueous fluid connectivity in the mantle wedge, *Nature,* **401,** 259–262.

Moore, D.E. & Lockner, D.A., 2007. Comparative deformation behavior of minerals in serpentinized ultramafic rock: Application to the slab-mantle interface in subduction zones, *Int. Geol. Rev.,* **49,** 401–415.

Norabuena, E. *et al.*, 2004. Geodetic and seismic constraints on some seismogenic zone processes in Costa Rica, *J. geophys. Res.,* **109,** B11403, doi:10.1029/2003JB002931.

Park, J., Lindbergh, C.R. & Vernon, F.L., III., 1987. Multitaper spectral analysis of high-frequency seismograms, *J. geophys. Res.,* **92,** 12 675–612 684.

Peacock, S.M., Van Keken, P.E., Holloway, S.D., Hacker, B.R., Abers, G.A. & Fergason, R.L., 2005. Thermal structure of the Costa Rica-Nicaragua subduction zone, *Phys. Earth planet. Inter.,* **149,** 187–200.

Percival, D.B. & Walden, A.T., 1998. *Spectral Analysis for Physical Applications,* Cambridge University Press, Cambridge.

Protti, M., Gundel, F. & McNally, K., 1994. The geometry of the Wadati-Benioff zone under southern Central America and its tectonic significance: results from a high-resolution local seismographic network, *Phys. Earth planet. Inter.,* **84,** 271–287.

Protti, M. *et al.*, 1995. The March 25, 1990 (Mw = 7.0, ML = 6.8), earthquake at the entrance of the Nicoya Gulf, Costa Rica: its prior activity, foreshocks, aftershocks, and triggered seismicity, *J. geophys. Res.,* **100,** 20 345–320 358.

Quintero, R. & Güendel, F., 2000. Stress field in Costa Rica, Central America, *J. Seismol.,* **4,** 297–319, doi:10.1023/A:1009867405248.

Ranero, C.R., Phipps Morgan, J., McIntosh, K. & Reichert, C., 2003. Bending-related faulting and mantle serpentinization at the Middle America Trench, *Nature,* **425,** 367–373.

Ranero, C.R. *et al.*, 2008. Hydrogeological system of erosional convergent margins and its influence on tectonics and interplate seismogenesis, *Geochem. Geophys. Geosyst.,* **9,** Q03S04, doi:10.1029/2007GC001679.

Rüpke, L.H., Phipps Morgan, J., Hort, M. & Connolly, J.A.D., 2004. Serpentine and the subduction zone water cycle, *Earth planet. Sci. Lett.,* **223,** 17–34.

Rychert, C.A., Fischer, K.M., Abers, G.A., Plank, T., Syracuse, E.M., Protti, J.M., Gonzalez, V. & Strauch, W., 2008. Strong along-arc variations in attenuation in the mantle wedge beneath Costa Rica and Nicaragua, *Geochem. Geophys. Geosyst.,* **9,** Q10S10, doi:10.1029/2008GC002040.

Sak, P.B., Fisher, D.M., Gardner, T.W., Marshall, J.S. & LaFemina, P.C., 2009. Rough crust subduction, forearc kinematics, and Quaternary uplift rates, Costa Rican segment of the Middle American Trench, *Geol. Soc. Am. Bull.,* **121,** 992–1012, doi:10.1130/B26237.1.

Sallarès, V. & Charvis, P., 2003. Crustal thickness constraints on the geodynamic evolution of the Galapagos Volcanic Province, *Earth planet. Sci. Lett.,* **214,** 545–559.

Sallarès, V., Dañobeitia, J.J. & Flueh, E.R., 2001. Lithospheric structure of the Costa Rican Isthmus: Effects of subduction zone magmatism on an oceanic plateau, *J. geophys. Res.,* **106,** 621–644.

Sallarès, V., Charvis, P., Flueh, E.R. & Bialas, J., 2003. Seismic structure of Malpelo and Cocos Volcanic Ridges and implications for hotspot-ridge interaction, *J. geophys. Res.,* **108,** 2564, doi:10.1029/2003JB002431.

Sato, T. & Hirasawa, T., 1973. Body wave spectra from propagating shear cracks, *J. Phys. Earth,* **21,** 415–431.

Schmidt, M.W. & Poli, S., 1998. Experimentally based water budgets for dehydrating slabs and consequences for arc magma generation, *Earth planet. Sci. Lett.,* **163,** 361–379.

Schnabel, M., Flueh, E.R., Klaeschen, D. & Zillmer, M., 2007. AVA analysis reveals in situ sediment diagenesis at the Costa Rican décollement, *Sed. Geol.,* **196,** 269–277.

Shelly, D.R., Beroza, G.C., Ide, S. & Nakamula, S., 2006. Low-frequency earthquakes in Shikoku, Japan, and their relationship to episodic tremor and slip, *Nature,* **442,** 188–191, doi:10.1038nature04931.

Song, T.-R.A., Helmberger, D.V., Brudzinski, M.R., Clayton, R.W., Davis, P., Pérez-Campos, X. & Singh, S.K., 2009. Subducting slab ultra-slow velocity layer coincident with silent earthquakes in southern Mexico, *Science,* **324,** 502–506, doi:10.1126/science.1167595.

Spandler, C., Hermann, J., Arculus, R. & Mavrogenes, J., 2003. Redistribution of trace elements during prograde metamorphism from lawsonite blueschist to eclogite facies; implications for deep subduction-zone processes, *Cont. Mineral. Petrol.,* **146,** 205–222.

Stachnik, J.C., Abers, G.A. & Christensen, D.H., 2004. Seismic attenuation and mantle wedge temperatures in the Alaska subduction zone, *J. geophys. Res.,* **109,** B10304, doi:10.1029/2004JB003018.

Syracuse, E.M. & Abers, G.A., 2006. Global compilation of variations in slab depth beneath arc volcanoes and implications, *Geochem. Geophys. Geosyst.,* **7,** Q05017, doi:10.1029/2005GC001045.

Syracuse, E.M., Abers, G.A., Fischer, K., MacKenzie, L., Rychert, C., Protti, M., González, V. & Strauch, W., 2008. Seismic tomography and earthquake locations in the Nicaraguan and Costa Rican upper mantle, *Geochem. Geophys. Geosyst.,* **9,** Q07S08, doi:10.1029/2008GC001963.

Toksöz, M.N., Mandal, B. & Dainty, A.M., 1990. Frequency dependent attenuation in the crust, *Geophys. Res. Lett.,* **17,** 973–976.

Vannucchi, P., Fisher, D.M., Bier, S. & Gardner, T.W., 2006. From seamount accretion to tectonic erosion: Formation of Osa Mélange and the effects of Cocos Ridge subduction in southern Costa Rica, *Tectonics,* **25,** TC2004, doi:10.1029/2005TC001855.

Vannucchi, P., Ranero, C.R., Galeotti, S., Straub, S.M., Scholl, D.W. & McDougall-Ried, K., 2003. Fast rates of subduction erosion along the Costa Rica Pacific margin: implications for nonsteady rates of crustal recycling at subduction zones, *J. geophys. Res.,* **108,** 2511, doi:10.1029/2002JB002207.

Vogel, T.A., Patino, L.C., Alvarado, G.E. & Gans, P.B., 2004. Silicic ignimbrites within the Costa Rican volcanic front: evidence for the formation of continental crust, *Earth planet. Sci. Lett.,* **226** 149–159.

von Huene, R., Ranero, C.R., Weinrebe, W. & Hinz, K., 2000. Quarternary convergent margin tectonics of Costa Rica, segmentation of the Cocos plate, and Central American volcanism, *Tectonics,* **19,** 314–334.

von Huene, R., Ranero, C.R. & Vannucchi, P., 2004. Generic model of subduction erosion, *Geology,* **32,** 913–916, doi:10.1130/G20563.1.

Wada, I., Wang, K., He, J. & Hyndman, R.D., 2008. Weakening of the subduction interface and its effects on surface heat flow, slab dehydration, and mantle wedge serpentinization, *J. geophys. Res.,* **113,** B04402, doi:10.1029/2007JB005190.

Walther, C.H.E., 2003. The crustal structure of the Cocos Ridge off Costa Rica, *J. geophys. Res.,* **108,** 2136, doi:10.1029/2001JB000888.

Ye, S., Bialas, J., Flueh, E.R., Stavenhagen, A. & von Huene, R., 1996. Crustal structure of the Middle American Trench off Costa Rica from wide-angle seismic data, *Tectonics,* **15,** 1006–1021.

Zhu, J., Kopp, H., Flueh, E.R., Klaeschen, D., Papenberg, C. & Planert, L., 2009. Crustal structure of the central Costa Rica subduction zone: implications for basal erosion from seismic wide-angle data, *Geophys. J. Int.,* **178,** 1112–1131, doi:10.1111/j.1365-246X.2009.04208.x.